AIMS Mathematics, 11(11): 39040–39074.
DOI: 10.3934/math.20261504
Received: 12 September 2026
Revised: 03 November 2026
Accepted: 06 November 2026
Published: 23 November 2026

https://www.aimspress.com/journal/Math

Research article

Modeling quarantine and isolation strategies for lumpy skin disease using an SEIQTR deep neural network framework

Ebraheem Alzahrani[1], Rubiqa Zulfiqar[2], Abdul Mannan[3] and Muhammad Farhan Hanif[4,5,*]

[1] Department of Mathematics, Faculty of Science, King Abdulaziz University, Jeddah, Saudi Arabia

[2] Department of Mathematics and Statistics, University of Lahore, Lahore 54000, Pakistan

[3] Abdus Salam School of Mathematical Sciences, Government College University, Lahore 54000, Pakistan

[4] Department of Mathematics, King Fahd University of Petroleum and Minerals, Dhahran 31261, Saudi Arabia

[5] Interdisciplinary Center of Smart Mobility and Logistics, King Fahd University of Petroleum and Minerals, Dhahran 31261, Saudi Arabia

* **Correspondence:** Email: farhanlums@gmail.com.

Abstract: Lumpy skin disease is a vector-borne viral disease of cattle that causes substantial economic losses through reduced milk production, reproductive problems, treatment costs, and death. In this study, we develop a novel integrated susceptible–exposed–infectious–quarantined–treated–recovered (SEIQTR)–deep neural network (DNN) framework to explore the transmission and control of lumpy skin disease. Cattle are divided into susceptible, exposed, infectious, quarantined, treated, and recovered compartments. The model separates the quarantine of exposed cattle from the isolation and treatment of infectious cattle, allowing the two interventions to be compared. Existence, uniqueness, non-negativity, and boundedness of the solutions are established. The disease-free and endemic equilibria are determined, and the basic reproduction number $\mathcal{R}_0$ is derived by the next-generation matrix method. When $\mathcal{R}_0 < 1$, the disease-free equilibrium is locally and globally asymptotically stable; when $\mathcal{R}_0 > 1$, there exists a unique biologically feasible endemic equilibrium. A sensitivity analysis shows that the transmission rate and the quarantine and isolation rates are the parameters that most strongly affect the persistence of the disease. Numerical experiments show that strengthening quarantine and isolation together reduces the prevalence of infection and $\mathcal{R}_0$ more than either measure alone. In addition, a feed-forward deep neural network trained on fourth-order Runge–Kutta solutions reproduces the nonlinear temporal behavior of all six compartments with coefficients of determination above 0.998 and relative L^2 errors below 3.2×10^{-2} on held-out test data. The proposed framework is a computationally efficient tool for assessing control strategies and highlights the importance of prompt quarantine and isolation in reducing lumpy skin disease outbreaks.

Keywords: infectious disease; deep neural networks; lumpy skin disease; SEIQTR model; quarantine and isolation; Runge–Kutta method
Mathematics Subject Classification: 92D30, 34D23, 68T07, 65L06

1. Introduction

Lumpy skin disease (LSD) is an acute-to-subacute viral disease of cattle whose clinical signature is a crop of firm, circumscribed cutaneous nodules [1]. The current classification of such viruses is given in the ICTV virus taxonomy profile of the family *Poxviridae* [2]. The causative agent, lumpy skin disease virus (LSDV), is a double-stranded DNA virus of roughly 150 kb assigned to the genus *Capripoxvirus* (subfamily *Chordopoxvirinae*, family *Poxviridae*), a genus that also contains the sheeppox and goatpox virus [3]. Cattle and water buffalo are the natural hosts, and transmission occurs predominantly by mechanical carriage on the mouthparts of hematophagous arthropods—stable flies, mosquitoes, ticks, and *Culicoides* midges—rather than by an obligate biological cycle in the vector [4]. Experimental studies have examined the mechanical transmission of LSDV by biting insects in detail [5]. Secondary routes matter as well: Suckling calves may acquire infection through milk, and virus shed in saliva can contaminate communal feed and water points [6]. The virus has also been detected in the saliva of ticks fed on infected cattle [7].

The epidemiological importance of LSD is inseparable from the economic weight of the sector it attacks. Livestock production underpins rural livelihoods and a substantial share of gross domestic product in many low- and middle-income economies [8]. The epidemiology and economic importance of LSD in such economies, including its effect on trade and on the productivity of cattle, have been reviewed in detail [9]. Livestock is also central to food security, to poverty reduction, and to wealth creation in many regions, as documented for West Africa [10]. The diverse and complex roles that animal species play in human societies around the world have been reviewed by Alders et al. [11]. An LSD incursion reduces milk yield sharply, causes abortion and temporary or permanent infertility, and produces hide damage, emaciation, and occasional death [12]. LSD outbreaks have also been investigated in Ethiopia, including virus isolation and molecular detection [13]. Because the disease spreads across national borders with animal movement and trade, the World Organisation for Animal Health lists it as notifiable [14].

Compartmental models remain the standard quantitative instrument for turning such biological narratives into testable statements about outbreak size, timing, and controllability, as a systematic review of LSD modeling has shown [15]. In a mathematical study of LSD, Butt et al. formulated a compartmental model and analyzed the optimal control of the disease through vaccination [16]. Alfwzan et al. proposed a novel mathematical study to understand the transmission of LSD and to assess the factors that drive its spread in cattle populations [17]. The general theory of mathematical modeling of infectious disease dynamics is well established and has been reviewed by Siettos and Russo [18]. A systematic introduction to the mathematical modeling of infectious diseases, covering model formulation, analysis, and applications, is given by Li [19]. The same machinery has been deployed for Marburg virus transmission with quarantine and health-awareness interventions using a deep-learning-driven approach [20]. It has also been applied to the outbreak of COVID-19, including

the loss of immunity and a quarantined class, through numerical simulation [21]. A new intervention strategy for HIV/AIDS transmission has been designed by combining general fractional modeling with an optimal control approach [22]. Optimal chemoprophylaxis and treatment control strategies have been derived for a tuberculosis transmission model by Agusto [23]. The effect of quarantine on the transmission dynamics of the Ebola virus epidemic has been examined through a detailed mathematical analysis [24]. Ebola virus disease with a nonlinear incidence rate has also been studied using Morlet wavelet neural networks and hybrid optimization techniques [25]. A new and generalized fractional model has been fitted to a real cholera outbreak to describe its course and to compare control options [26]. A Caputo–Fabrizio fractional model of COVID-19 has been analyzed theoretically to determine how the spread of the pandemic can be optimally controlled [27]. The COVID-19 epidemic has also been investigated computationally using wavelet neural networks together with coupled optimization procedures [28]. The value of this machinery lies in allowing an intervention to be evaluated before it is financed.

Recent advances in epidemic modeling have examined how network structure, population turnover, and behavioral responses shape transmission. Li et al. [29] coupled awareness-based, event-triggered migration with epidemic spreading in networked cyber-physical systems. Feng et al. [30] modeled transmission on a birth–death evolving network that includes indirect contacts. Peng et al. [31] analyzed coupled information-epidemic dynamics on hypergraphs that account for interpersonal relationships. These studies are relevant to the present framework in three respects: indirect and environment- or vector-mediated contact is also the dominant route of LSD transmission; demographic turnover enters the present model through the recruitment and natural mortality rates Λ and μ; and awareness-driven responses are the practical mechanism through which quarantine and isolation are triggered. They differ from the present work, however, in that they resolve contact structure at the level of individuals, networks, or hypergraphs, whereas intervention is not separated according to the infection stage at which it acts. The novelty of the present study lies in this stage-specific representation of control: The quarantine of exposed cattle and isolation of infectious cattle are modeled as separate pathways, their individual contributions to the basic reproduction number are quantified analytically, and the resulting susceptible–exposed–infectious–quarantined–treated–recovered (SEIQTR) system is coupled with a deep neural network (DNN) trained on fourth-order Runge–Kutta (RK4)-generated trajectories, combining mathematical analysis of transmission dynamics with efficient numerical approximation of the resulting system.

Existing LSD models are, with few exceptions, of susceptible–exposed–infectious–recovered (SEIR) type. Falowo et al. developed a mathematical model of LSD in dairy cows and examined the conditions under which the infection persists [32]. Magori-Cohen et al. built a mathematical model to evaluate the relative contribution of the different routes of transmission of LSDV [33]. Mat et al. determined the production losses related to LSD among cattle in Turkey and analyzed the outbreak with an SEIR epidemic model [34]. These models have clarified how vector abundance, vaccination coverage, and seasonality shape outbreak potential, but they treat removal from the transmission chain as a single undifferentiated process. In field practice, however, it is not. Quarantining animals that have been exposed but are not yet infectious and isolating animals that are already shedding virus differ in detection cost; in the veterinary capacity they consume; and crucially, in the number of secondary infections they avert. A model that collapses the two cannot rank them. The first contribution of this paper is therefore an SEIQTR structure carrying two distinct removal rates, φ_E for exposed cattle and

φ_I for infectious cattle, feeding a common quarantine class Q that sits alongside a treatment class T.

Related numerical investigations have also considered alternative formulations of lumpy skin disease and biological systems. Sweilam et al. [35] examined numerical treatments for a crossover fractional LSD model. Furthermore, improved numerical schemes have been developed for general fractional diabetes models [36]. An efficient discretization scheme has also been proposed for a time-delay variable-order fractional diabetes model [37]. These studies provide methodological context for the present work, which considers an integer-order SEIQTR model which employs RK4-based numerical solutions together with a DNN surrogate.

The second contribution is computational. The resulting system is a set of six coupled, nonlinear ordinary differential equations (ODEs) with no closed-form solution, and repeated evaluation—for elasticity screening, scenario sweeps, or eventual optimal-control work—multiplies the cost of any step-based solver. Mesh-based schemes additionally accumulate truncation error and can become unstable on stiff or strongly nonlinear right-hand sides. Neural approximants sidestep the mesh entirely: They represent the state variables as smooth parametric functions of time and are therefore evaluable at any instant once trained, as reviewed in the overview of deep learning by LeCun et al. [38]. The foundations and main architectures of artificial neural networks are described in the textbook of Yegnanarayana [39]. Machine learning more broadly has been reviewed by Jordan and Mitchell in terms of its current trends, perspectives, and future prospects [40]. A comprehensive account of the theory and practice of deep learning is given in the monograph of Goodfellow et al. [41]. Neural methods are also central to modern computer vision, whose algorithms and applications are presented by Szeliski [42]. The state of the art in artificial neural network applications across many fields has been surveyed by Abiodun et al. [43]. Neural solvers for differential equations have matured rapidly since the trial-solution framework for ordinary and partial differential equations of Lagaris et al. [44]. Yadav et al. later gave a book-length introduction to neural network methods for ordinary and partial differential equations [45]. Parisi et al. showed that differential equations arising in chemical process engineering can be solved with unsupervised neural networks [46]. Mall and Chakraverty applied a single-layer Legendre neural network to the solution of ordinary differential equations [47]. Michoski et al. investigated the solution of differential equations, including shock-forming problems, using deep neural networks [48]. Kumar and Yadav surveyed the deep-learning algorithms that have been proposed for solving ordinary and partial differential equations [49]. Wang et al. used a deep neural network to solve partial differential equations with complex boundaries arising in groundwater seepage [50]. Zeroing neural networks, in particular, have been developed for time-varying problems with complex-valued and robust parameters [51]. Fuzzy-parameter zeroing neural networks have also been applied to the synchronization of chaotic systems [52].

Applications of deep networks now include epidemiological prediction from surveillance data, as shown by Wu et al. [53]. An oscillatory deep neural network has been developed to simulate the dynamics of coupled electrical circuits by Ul Rahman et al. [54]. The Sel'kov model of glycolysis has been simulated and comprehensively analyzed with deep neural networks [55]. A data-driven investigation of an epidemic model under a saturated incidence rate has been carried out using deep neural networks [56]. Deep neural networks have also been applied in mathematical epidemiology to the transmission dynamics of the rabies virus [57]. Marburg virus epidemics have been analyzed and modeled for health-care planning with an artificial neural network-based approach [58]. Protein-folding dynamics have been simulated with an environment-aware physics-informed neural network

called PhyFold [59]. The training objective is a loss functional measuring the mismatch between network output and reference dynamics. Loss functions for deep neural networks in classification have been compared by Janocha and Czarnecki [60]. A comprehensive survey of the loss functions used across machine learning tasks is given by Wang et al. [61]. The mean absolute error has been analyzed as a loss for deep neural network-based vector-to-vector regression by Qi et al. [62]. An L_2-loss has been used in a nonparallel bounded support vector machine for robust classification by Liu et al. [63]. A unit softmax loss with Laplacian smoothing has been proposed for training deep convolutional neural networks [64]. Mean squared error and Huber losses are also standard candidates. Here, an optimized feed-forward network is trained against RK4 trajectories and validated compartment by compartment.

It is worth distinguishing the present use of deep learning from image-based approaches developed for LSD detection. For example, Selvam et al. [65] proposed an automated framework that combines image enhancement, Gabor-wavelet feature extraction, and deep learning classifiers to identify LSD-infected cattle from images. In contrast, the present study does not aim to classify clinical images or diagnose individual animals. Instead, the DNN is employed as a numerical surrogate for the proposed SEIQTR transmission model, approximating its six compartmental trajectories from RK4-generated solutions. The contribution therefore lies in integrating epidemiological transmission modeling, explicit representation of quarantine and treatment interventions, and neural-network-based numerical approximation.

More broadly, machine-learning and deep-learning tools are increasingly used across biomedical and disease-related research. Wang et al. [66] combined meta-analysis with machine learning to evaluate a therapeutic strategy for liver diseases. Liu et al. [67] predicted human microbe–disease associations through nuclear-norm minimization. Du et al. [68] integrated network pharmacology, molecular docking, and molecular dynamics to investigate therapeutic action in myocarditis. For outbreak control, Wang et al. [69] proposed a proactive early-warning system and treatment strategy for monkeypox prevention. Deep networks have also been applied to imaging and sensing data. Qian et al. [70] used ensemble deep learning for structured illumination microscopy. Pan et al. [71] developed unmanned aerial vehicle (UAV)-based detection of fish disease. Chi et al. [72] applied deep learning to fouling detection in engineering inspection. These studies are predominantly data-driven, learning associations, classifications, or predictions directly from observations. The present work is complementary: The neural network is trained on solutions of a mechanistic transmission model so that its outputs remain interpretable in terms of epidemiological compartments and intervention parameters.

The remainder of the paper is organized as follows. Section 2 sets out the SEIQTR system and its parameters. Section 3 establishes well-posedness and the invariant region. Section 4 derives both equilibria and $\mathcal{R}_0$, and Section 5 settles local and global stability of the disease-free state. Section 6 reports the elasticity analysis together with surface and contour diagnostics. Section 7 describes the neural framework, and Section 8 presents a numerical comparison and scenario study. Sections 9 and 10 discuss and conclude.

2. Model formulation

A cattle herd at time t is partitioned into six mutually exclusive epidemiological states: susceptible $S(t)$, exposed (latently infected, not yet infectious) $E(t)$, infectious $I(t)$, quarantined $Q(t)$, under

treatment $T(t)$, and recovered $R(t)$ so that the herd size is

$$N(t) = S(t) + E(t) + I(t) + Q(t) + T(t) + R(t). \tag{2.1}$$

Recruitment into the susceptible class occurs at the constant rate Λ. Susceptible animals acquire infection through effective contact with infectious animals, described by the standard incidence $\beta S I/N$; the use of a frequency-dependent term reflects the fact that vector-mediated contact saturates with herd size rather than growing linearly with it. Newly infected animals enter E, where they harbor the virus but do not transmit, and leave it at rate σ towards I or at rate φ_E towards quarantine. Infectious animals leave I along four channels: natural recovery at rate γ, entry into treatment at rate θ, isolation at rate φ_I, and disease-induced death at rate δ_I. Quarantined and treated animals recover at rates ψ and ω and die of disease at rates δ_Q and δ_T, respectively. Every compartment is subject to the natural mortality rate μ. The transfer structure is displayed in Figure 1, and the governing system reads

$$\frac{\mathrm{d}S}{\mathrm{d}t} = \Lambda - \beta\frac{SI}{N} - \mu S, \tag{2.2}$$

$$\frac{\mathrm{d}E}{\mathrm{d}t} = \beta\frac{SI}{N} - (\sigma + \mu + \varphi_E)E, \tag{2.3}$$

$$\frac{\mathrm{d}I}{\mathrm{d}t} = \sigma E - (\gamma + \mu + \delta_I + \theta + \varphi_I)I, \tag{2.4}$$

$$\frac{\mathrm{d}Q}{\mathrm{d}t} = \varphi_E E + \varphi_I I - (\psi + \mu + \delta_Q)Q, \tag{2.5}$$

$$\frac{\mathrm{d}T}{\mathrm{d}t} = \theta I - (\omega + \mu + \delta_T)T, \tag{2.6}$$

$$\frac{\mathrm{d}R}{\mathrm{d}t} = \gamma I + \omega T + \psi Q - \mu R, \tag{2.7}$$

subject to the non-negative initial data

$$\begin{aligned} &S(0) = S_0 \geq 0, \quad &&E(0) = E_0 \geq 0, \quad &&I(0) = I_0 \geq 0, \\ &Q(0) = Q_0 \geq 0, \quad &&T(0) = T_0 \geq 0, \quad &&R(0) = R_0 \geq 0. \end{aligned} \tag{2.8}$$

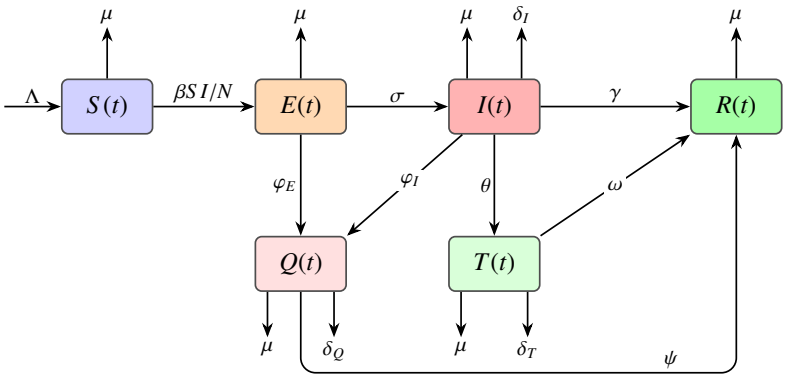

Figure 1. Transfer diagram of the SEIQTR model (2.2)–(2.7). Exposed cattle are quarantined at rate φ_E, and infectious cattle are isolated at rate φ_I; both flows feed the same class Q but act at different stages of the infection.

Throughout the paper, the following composite constants are used; they collect the total per-capita exit rates from the four infected classes and shorten every subsequent formula:

$$\begin{aligned} m_1 &= \sigma + \mu + \varphi_E, & m_2 &= \gamma + \mu + \delta_I + \theta + \varphi_I, \\ m_3 &= \psi + \mu + \delta_Q, & m_4 &= \omega + \mu + \delta_T. \end{aligned} \tag{2.9}$$

All parameters in (2.2)–(2.7) are assumed positive, which is the standing hypothesis for every result below. The interpretation, baseline value, and source of each parameter are listed in Table 1. To distinguish the effects of quarantine and isolation on disease transmission, the proposed model incorporates separate pathways for exposed and infectious cattle. As reliable LSD-specific estimates for these intervention rates were not identified in the available sources, $\varphi_E = 0.30$ and $\varphi_I = 0.40$ have been adopted as illustrative values. The quarantine recovery rate $\psi = 0.20$ is chosen between the recovery rates $\omega = 0.055$ and $\gamma = 0.30$, and the disease-induced mortality rate $\delta_Q = 0.03$ is taken equal to δ_I. These assumptions provide a baseline for the numerical investigation, and their influence on the model outcomes is further examined through the robustness analysis in Section 6.2.

All rates are expressed per day, and all compartments are measured in numbers of animals. The natural mortality rate $\mu = 0.0001261$ day^{-1} corresponds to an average residence time in the herd of $1/\mu \approx 7930$ days (about 21.7 years) [73], and the recruitment rate is fixed by the demographic balance $\Lambda = \mu N^0 = 0.8827$ animals per day. With this scaling, the disease-free herd size $N^0 = \Lambda/\mu = 7000$ coincides with the total initial population used in the numerical experiments of Section 8, so the demographic parameters and the simulated herd are mutually consistent. All baseline values used in this study are summarized in Table 1.

Table 1. State variables and parameters of the SEIQTR model. Rates are expressed per day.

Symbol	Interpretation	Baseline	Source
S, E, I	Susceptible, exposed (latent), infectious cattle	—	—
Q, T, R	Quarantined, treated, recovered cattle	—	—
Λ	Recruitment rate into the susceptible class	0.8827	Derived $\Lambda = \mu N^0$
β	Effective transmission coefficient ($S \to E$)	0.032	[74]
σ	Progression rate from latency to infectiousness ($E \to I$)	0.59	[74]
γ	Natural recovery rate of infectious cattle ($I \to R$)	0.3	[16]
θ	Rate at which infectious cattle enter treatment ($I \to T$)	0.03	[75]
ω	Recovery rate of treated cattle ($T \to R$)	0.055	[75]
ψ	Recovery rate of quarantined cattle ($Q \to R$)	0.2	Assumed
φ_E	Quarantine rate of exposed cattle ($E \to Q$)	0.30	Assumed
φ_I	Isolation rate of infectious cattle ($I \to Q$)	0.40	Assumed
δ_I	Disease-induced mortality rate in I	0.03	[75]
δ_T	Disease-induced mortality rate in T	0.03	[75]
δ_Q	Disease-induced mortality rate in Q	0.03	Assumed
μ	Natural mortality rate	0.0001261	[73]
$m_1, \ldots, m_4$	Composite exit rates defined in (2.9)	—	—
$\mathcal{R}_0$	Basic reproduction number, Eq (4.4)	0.0279	This study

3. Well-posedness of the model

Before any dynamical conclusion is drawn, the system must be shown to define a genuine population model: Solutions have to exist, be unique, stay non-negative, and stay bounded. Writing $z(t) = \big(S(t), E(t), I(t), Q(t), T(t), R(t)\big)^{\top}$, the system (2.2)–(2.7) is the initial value problem

$$\frac{\mathrm{d}z}{\mathrm{d}t} = \mathcal{G}(z(t)), \qquad z(0) = z_0 \in \mathbb{R}^6_+, \tag{3.1}$$

with $\mathcal{G} = (\mathcal{G}_1, \ldots, \mathcal{G}_6)^{\top} : \mathbb{R}^6_+ \to \mathbb{R}^6$ given by

$$\begin{aligned} \mathcal{G}_1(z) &= \Lambda - \beta\frac{SI}{N} - \mu S, & \mathcal{G}_4(z) &= \varphi_E E + \varphi_I I - m_3 Q, \\ \mathcal{G}_2(z) &= \beta\frac{SI}{N} - m_1 E, & \mathcal{G}_5(z) &= \theta I - m_4 T, \\ \mathcal{G}_3(z) &= \sigma E - m_2 I, & \mathcal{G}_6(z) &= \gamma I + \omega T + \psi Q - \mu R. \end{aligned} \tag{3.2}$$

3.1. Existence and uniqueness

Theorem 3.1. *Let $\mathcal{T} > 0$, and let $\mathbb{V} \subset \mathbb{R}^6_+$ be compact and convex with $N \geq N_{\min} > 0$ on $\mathbb{V}$. Then, $\mathcal{G}$ is Lipschitz continuous on $\mathbb{V}$, and consequently, the initial value problem* (3.1) *possesses exactly one solution on* $[0, \mathcal{T}]$.

Proof. Every component in (3.2) is a polynomial in the state variables except for the incidence term $\beta SI/N$, which is a rational function whose denominator is bounded away from zero on $\mathbb{V}$ by hypothesis. Hence, $\mathcal{G} \in C^1(\mathbb{V})$, and all first-order partial derivatives are continuous on the compact set $\mathbb{V}$ so that

$$L := \sup_{z \in \mathbb{V}} \big\|\mathcal{G}'(z)\big\| < \infty.$$

Take $z_1, z_2 \in \mathbb{V}$. Convexity guarantees that the segment joining them lies in $\mathbb{V}$, so the mean value inequality applied along that segment yields

$$\big\|\mathcal{G}(z_1) - \mathcal{G}(z_2)\big\| \leq \sup_{\xi \in [z_1, z_2]} \big\|\mathcal{G}'(\xi)\big\| \, \big\|z_1 - z_2\big\| \leq L \, \big\|z_1 - z_2\big\|.$$

Thus, $\mathcal{G}$ is globally Lipschitz on $\mathbb{V}$ with constant L, and the Picard–Lindelöf theorem delivers a unique solution of (3.1) on $[0, \mathcal{T}]$. □

3.2. Non-negativity of solutions

Theorem 3.2. *For non-negative initial data* (2.8)*, the solution of* (2.2)–(2.7) *satisfies that all six components remain non-negative for every $t \geq 0$; the non-negative orthant $\mathbb{R}^6_+$ is therefore forward invariant.*

Proof. Equation (2.2) can be written as $\dot{S} = \Lambda - \Phi(t)S$ with $\Phi(t) = \beta I(t)/N(t) + \mu$. Multiplying by the integrating factor $\exp\big(\int_0^t \Phi(s)\,\mathrm{d}s\big)$ and integrating from 0 to t gives

$$S(t) = S_0 \exp\Big(-\int_0^t \Phi(s)\,\mathrm{d}s\Big) + \Lambda \int_0^t \exp\Big(-\int_u^t \Phi(s)\,\mathrm{d}s\Big)\mathrm{d}u \;\geq\; 0$$

because $S_0 \geq 0$, $\Lambda > 0$, and the exponentials are strictly positive. The remaining equations are treated identically. Each has the form $\dot{X} = g_X(t) - h_X(t)X$ with $g_X \geq 0$ whenever the compartments feeding X are non-negative, namely

$$g_E = \beta S I/N, \quad g_I = \sigma E, \quad g_Q = \varphi_E E + \varphi_I I,$$
$$g_T = \theta I, \qquad g_R = \gamma I + \omega T + \psi Q,$$

and the corresponding decay coefficients are the positive constants m_1, m_2, m_3, m_4, and μ. The same integrating-factor representation therefore yields $E(t), I(t), Q(t), T(t), R(t) \geq 0$ for all $t \geq 0$. Formally, if the conclusion failed, there would be a first time $t^\star > 0$, at which some component would vanish and be about to become negative; at that instant, its derivative would equal $g_X(t^\star) \geq 0$, which contradicts a strict decrease through zero. □

3.3. Boundedness and the invariant region

Theorem 3.3. *Every solution of* (2.2)–(2.7) *with non-negative initial data is bounded, and the set*

$$\Gamma = \left\{(S, E, I, Q, T, R) \in \mathbb{R}^6_+ : \ N \leq \frac{\Lambda}{\mu}\right\} \tag{3.3}$$

is compact and positively invariant; it attracts all solutions starting in $\mathbb{R}^6_+$.

Proof. Summing (2.2)–(2.7) and using (2.1),

$$\frac{\mathrm{d}N}{\mathrm{d}t} = \Lambda - \mu N - \delta_I I - \delta_T T - \delta_Q Q. \tag{3.4}$$

By Theorem 3.2, the three loss terms are non-negative; hence, $\dot{N} \leq \Lambda - \mu N$. Grönwall's inequality applied to this differential inequality gives

$$N(t) \leq \frac{\Lambda}{\mu} + \Big(N(0) - \frac{\Lambda}{\mu}\Big)e^{-\mu t}, \qquad t \geq 0,$$

so that $\limsup_{t\to\infty} N(t) \leq \Lambda/\mu$, and $N(t) \leq \Lambda/\mu$ for all $t \geq 0$ whenever $N(0) \leq \Lambda/\mu$. Because every compartment is non-negative, and their sum is N, each of them is bounded above by Λ/μ. Consequently, no trajectory can leave Γ, and trajectories starting outside Γ approach it asymptotically. The model is thus mathematically and biologically well posed on Γ, and all subsequent analysis is carried out there. □

Remark 3.4. Restricting the dynamics to Γ also removes the only singularity of the vector field: On Γ with $N(0) > 0$, one has $N(t) \geq \min\{N(0), \Lambda/\mu\}e^{-(\mu+\max\{\delta_I,\delta_T,\delta_Q\})t} > 0$, so the standard incidence $\beta S I/N$ is smooth, and Theorem 3.1 applies on every compact time interval.

4. Equilibria and the reproduction number

Steady states are the solutions of

$$\begin{aligned} \Lambda - \beta\frac{SI}{N} - \mu S &= 0, & \varphi_E E + \varphi_I I - m_3 Q &= 0, \\ \beta\frac{SI}{N} - m_1 E &= 0, & \theta I - m_4 T &= 0, \\ \sigma E - m_2 I &= 0, & \gamma I + \omega T + \psi Q - \mu R &= 0. \end{aligned} \tag{4.1}$$

4.1. Disease-free equilibrium

Putting $I = 0$ in (4.1) forces $E = Q = T = R = 0$ and $S = \Lambda/\mu$, so the model possesses the unique disease-free equilibrium (DFE)

$$\mathcal{E}^0 = (S^0, E^0, I^0, Q^0, T^0, R^0) = \Big(\frac{\Lambda}{\mu}, 0, 0, 0, 0, 0\Big), \tag{4.2}$$

at which the whole herd is susceptible, and $N^0 = S^0 = \Lambda/\mu$.

4.2. Basic reproduction number

The threshold quantity $\mathcal{R}_0$ counts the secondary infections generated by one typical infectious animal introduced into an entirely susceptible herd. It is computed by the next-generation operator [76]. Ordering the infected states as (E, I, Q, T), the vector of new infections and the vector of remaining transfers are

$$\mathfrak{F} = \begin{pmatrix} \beta S I/N \\ 0 \\ 0 \\ 0 \end{pmatrix}, \qquad \mathfrak{V} = \begin{pmatrix} m_1 E \\ m_2 I - \sigma E \\ m_3 Q - \varphi_E E - \varphi_I I \\ m_4 T - \theta I \end{pmatrix}.$$

Their Jacobians evaluated at $\mathcal{E}^0$, where $S^0/N^0 = 1$, are

$$\boldsymbol{F} = \begin{pmatrix} 0 & \beta & 0 & 0 \\ 0 & 0 & 0 & 0 \\ 0 & 0 & 0 & 0 \\ 0 & 0 & 0 & 0 \end{pmatrix}, \qquad \boldsymbol{V} = \begin{pmatrix} m_1 & 0 & 0 & 0 \\ -\sigma & m_2 & 0 & 0 \\ -\varphi_E & -\varphi_I & m_3 & 0 \\ 0 & -\theta & 0 & m_4 \end{pmatrix}. \tag{4.3}$$

Because $\boldsymbol{V}$ is lower triangular with a positive diagonal, it is invertible, and the spectral radius of the next-generation matrix $\boldsymbol{F}\boldsymbol{V}^{-1}$ gives

$$\mathcal{R}_0 = \rho(\boldsymbol{F}\boldsymbol{V}^{-1}) = \frac{\beta\sigma}{m_1 m_2} = \frac{\beta\sigma}{(\sigma + \mu + \varphi_E)(\gamma + \mu + \delta_I + \theta + \varphi_I)}. \tag{4.4}$$

The interpretation is transparent: β/m_2 is the number of contacts an infectious animal makes before leaving I by any route, and σ/m_1 is the probability that an exposed animal survives latency without being quarantined and becomes infectious. Both quarantine rates enter the denominator, so each of them shortens exactly one of these two windows.

Remark 4.1 (Quantitative reading of $\mathcal{R}_0$)**.** With the baseline values of Table 1, $m_1 = 0.8901261$, and $m_2 = 0.7601261$, and hence, $\mathcal{R}_0 \approx 0.0279$. Setting $\varphi_E = \varphi_I = 0$ while keeping every other parameter fixed gives the quarantine-free counterpart

$$\mathcal{R}_0^{\text{free}} = \frac{\beta\sigma}{(\sigma + \mu)(\gamma + \mu + \delta_I + \theta)} \approx 0.088839,$$

so the joint quarantine effort reduces the reproduction number by about 68.6%. Conversely, holding the remaining parameters at baseline, the herd sustains transmission only if the transmission coefficient

exceeds the critical value $\beta^\star = m_1 m_2/\sigma \approx 1.146793$ day^{-1}. For a given $\beta > \beta^\star$, the isolation and quarantine efforts needed individually to return $\mathcal{R}_0$ to unity are

$$\varphi_I^c = \frac{\beta\sigma}{m_1} - (\gamma + \mu + \delta_I + \theta), \qquad \varphi_E^c = \frac{\beta\sigma}{m_2} - (\sigma + \mu),$$

which for $\beta = 2$ day^{-1} evaluate to $\varphi_I^c \approx 0.965528$ and $\varphi_E^c \approx 0.962248$ day^{-1}. Expressions of this type convert the threshold condition directly into a target for veterinary services.

4.3. Endemic equilibrium

Rather than solving (4.1) by brute-force elimination, which produces unwieldy expressions, we reduce the endemic state to a single scalar.

Proposition 4.2. *Define*

$$c_E = \frac{m_2}{\sigma}, \qquad c_Q = \frac{\varphi_E c_E + \varphi_I}{m_3}, \qquad c_T = \frac{\theta}{m_4}, \qquad c_R = \frac{\gamma + \omega c_T + \psi c_Q}{\mu}, \tag{4.5}$$

and put $\mathcal{A} = 1 + c_E + c_Q + c_T + c_R$. If $\mathcal{R}_0 > 1$, the model (2.2)–(2.7) *admits exactly one endemic equilibrium $\mathcal{E}^* = (S^*, E^*, I^*, Q^*, T^*, R^*)$ with*

$$\begin{gathered} I^* = \frac{\Lambda(\mathcal{R}_0 - 1)}{m_1 c_E(\mathcal{R}_0 - 1) + \mu\mathcal{A}}, \qquad S^* = \frac{\mathcal{A}}{\mathcal{R}_0 - 1} I^*, \\ E^* = c_E I^*, \qquad Q^* = c_Q I^*, \qquad T^* = c_T I^*, \qquad R^* = c_R I^*, \end{gathered} \tag{4.6}$$

and all six components are strictly positive. If $\mathcal{R}_0 \le 1$, no such equilibrium exists in Γ, and the DFE is the only steady state.

Proof. Assume $I^* \neq 0$. The third equation of (4.1) gives $E^* = c_E I^*$ with $c_E = m_2/\sigma$, and the fourth to sixth give $Q^* = c_Q I^*$, $T^* = c_T I^*$ and $R^* = c_R I^*$ with the coefficients (4.5). Substituting $E^* = c_E I^*$ into the second equation of (4.1) yields

$$\beta \frac{S^*}{N^*} I^* = m_1 c_E I^* = \frac{m_1 m_2}{\sigma} I^* \quad \Longrightarrow \quad \frac{S^*}{N^*} = \frac{m_1 m_2}{\beta\sigma} = \frac{1}{\mathcal{R}_0},$$

which is the familiar statement that at endemicity the susceptible fraction equals the inverse of the reproduction number. Writing $N^* = S^* + \mathcal{A} I^*$ and inserting $S^* = N^*/\mathcal{R}_0$ gives $S^*(1 - 1/\mathcal{R}_0) = \mathcal{A} I^*/\mathcal{R}_0$; that is, $S^* = \mathcal{A} I^*/(\mathcal{R}_0 - 1)$, which is admissible only for $\mathcal{R}_0 > 1$. Finally, adding the first two equations of (4.1) removes the incidence term and leaves $\Lambda = m_1 E^* + \mu S^*$; substituting $E^* = c_E I^*$ and $S^* = \mathcal{A} I^*/(\mathcal{R}_0 - 1)$ and solving for I^* produces (4.6). Because $\mathcal{A} > 0$, and all constants in (4.5) are positive, $I^* > 0$ precisely when $\mathcal{R}_0 > 1$, and then, every remaining component is positive, as well. Uniqueness is immediate: Each step above is an equivalence, so I^* is determined uniquely, and the other components are linear multiples of it. If $\mathcal{R}_0 \le 1$, the relation $S^* = \mathcal{A} I^*/(\mathcal{R}_0 - 1)$ cannot hold with both sides non-negative unless $I^* = 0$, which returns the DFE. □

Remark 4.3. Proposition 4.2 makes the threshold role of $\mathcal{R}_0$ structural rather than numerical: The endemic branch bifurcates from the DFE exactly at $\mathcal{R}_0 = 1$ and does so forwards, as I^* is an increasing function of $\mathcal{R}_0$ with $I^* \to 0^+$ as $\mathcal{R}_0 \to 1^+$. No backward bifurcation is possible in this model, which is consistent with the global stability result of Theorem 5.3. The closed form (4.6) is verified against long-time numerical integration of (2.2)–(2.7) and agrees to numerical precision.

5. Stability analysis

5.1. Local stability of the disease-free equilibrium

The Jacobian of (2.2)–(2.7), computed with N treated as the sum of the state variables and evaluated at the DFE where $S^0/N^0 = 1$, is the block-triangular matrix

$$\boldsymbol{J}(\mathcal{E}^0) = \begin{pmatrix} -\mu & 0 & -\beta & 0 & 0 & 0 \\ 0 & -m_1 & \beta & 0 & 0 & 0 \\ 0 & \sigma & -m_2 & 0 & 0 & 0 \\ 0 & \varphi_E & \varphi_I & -m_3 & 0 & 0 \\ 0 & 0 & \theta & 0 & -m_4 & 0 \\ 0 & 0 & \gamma & \psi & \omega & -\mu \end{pmatrix}. \tag{5.1}$$

Theorem 5.1. *The disease-free equilibrium $\mathcal{E}^0$ of Model* (2.2)–(2.7) *is locally asymptotically stable if $\mathcal{R}_0 < 1$ and unstable if $\mathcal{R}_0 > 1$.*

Proof. Expanding $\det(\boldsymbol{J}(\mathcal{E}^0) - \lambda \boldsymbol{I})$ along the first column and then along the columns corresponding to Q, T, and R shows that four eigenvalues are immediate,

$$\lambda_1 = \lambda_2 = -\mu, \qquad \lambda_3 = -m_3, \qquad \lambda_4 = -m_4,$$

all of which are negative because every parameter is positive. The two remaining eigenvalues are the roots of the characteristic polynomial of the (E, I) block,

$$\lambda^2 + (m_1 + m_2)\lambda + m_1 m_2(1 - \mathcal{R}_0) = 0, \tag{5.2}$$

obtained from $(\lambda + m_1)(\lambda + m_2) - \beta\sigma = 0$ together with (4.4). The coefficients of (5.2) are positive precisely when $\mathcal{R}_0 < 1$, so the Routh–Hurwitz criterion for a quadratic gives two roots with negative real part in that case, and $\mathcal{E}^0$ is locally asymptotically stable. If $\mathcal{R}_0 > 1$, the constant term is negative, the product of the roots is negative, and one real positive eigenvalue exists, so $\mathcal{E}^0$ is a saddle and hence unstable. □

Remark 5.2. Equation (5.2) corrects a coefficient that is easy to misassemble when the polynomial is expanded symbol by symbol: The linear coefficient is the sum $m_1 + m_2$ of both exit rates, not m_1 alone, because it is the trace of the (E, I) block. The threshold conclusion is unaffected, as the sign of the constant term alone decides stability.

5.2. Global stability of the disease-free equilibrium

Local analysis only controls small perturbations. The following result rules out any recurrence of the disease from arbitrarily large initial outbreaks within the feasible region.

Theorem 5.3. *If $\mathcal{R}_0 < 1$, the disease-free equilibrium $\mathcal{E}^0$ is globally asymptotically stable in* Γ.

Proof. We verify the two hypotheses of the Castillo–Chavez reduction. Split the state into the uninfected block $X = (S, R)$ and the infected block $Y = (E, I, Q, T)$, and write

$$\frac{\mathrm{d}X}{\mathrm{d}t} = \mathcal{P}(X, Y), \qquad \frac{\mathrm{d}Y}{\mathrm{d}t} = \mathcal{Q}(X, Y),$$

with

$$\mathcal{P}(X,Y)=\begin{pmatrix}\Lambda-\beta S\,I/N-\mu S\\ \gamma I+\omega T+\psi Q-\mu R\end{pmatrix},\qquad \mathcal{Q}(X,Y)=\begin{pmatrix}\beta S\,I/N-m_1E\\ \sigma E-m_2I\\ \varphi_E E+\varphi_I I-m_3Q\\ \theta I-m_4T\end{pmatrix}.$$

(H1) The reduced uninfected subsystem is globally stable. Setting $Y=0$ leaves $\dot{S}=\Lambda-\mu S$ and $\dot{R}=-\mu R$, a linear system whose unique equilibrium $X^0=(\Lambda/\mu,0)$ satisfies $\mathcal{P}(X^0,0)=0$ and attracts every solution, as $S(t)\to\Lambda/\mu$, and $R(t)\to 0$ exponentially at rate μ.

(H2) The infected subsystem is dominated by its linearization. Write $\mathcal{Q}(X,Y)=\mathfrak{M}Y-\widehat{\mathcal{Q}}(X,Y)$, where $\mathfrak{M}=D_Y\mathcal{Q}(X^0,0)=\boldsymbol{F}-\boldsymbol{V}$, with $\boldsymbol{F}$ and $\boldsymbol{V}$ given in (4.3),

$$\mathfrak{M}=\begin{pmatrix}-m_1 & \beta & 0 & 0\\ \sigma & -m_2 & 0 & 0\\ \varphi_E & \varphi_I & -m_3 & 0\\ 0 & \theta & 0 & -m_4\end{pmatrix}.$$

All off-diagonal entries of $\mathfrak{M}$ are non-negative, so $\mathfrak{M}$ is a Metzler matrix; it is also irreducible on the (E,I) block when $\beta>0$, and $\sigma>0$. Because $\mathcal{R}_0<1$ is equivalent to $\rho(\boldsymbol{F}\boldsymbol{V}^{-1})<1$, the matrix $\mathfrak{M}$ is Hurwitz, meaning that all its eigenvalues have strictly negative real parts. The remainder has the components

$$\widehat{\mathcal{Q}}_1(X,Y)=\beta I\Big(1-\frac{S}{N}\Big),\qquad \widehat{\mathcal{Q}}_2=\widehat{\mathcal{Q}}_3=\widehat{\mathcal{Q}}_4=0.$$

In Γ, one has $S\le N$, where $1-S/N\ge 0$, and $I\ge 0$ by Theorem 3.2; therefore, $\widehat{\mathcal{Q}}(X,Y)\ge 0$ componentwise for all $(X,Y)\in\Gamma$. Consequently, $\dot{Y}\le\mathfrak{M}Y$ componentwise. Because $\mathfrak{M}$ is Metzler and Hurwitz for $\mathcal{R}_0<1$, the comparison principle gives

$$0\le Y(t)\le e^{\mathfrak{M}t}Y(0).$$

As $e^{\mathfrak{M}t}\to 0$ when $t\to\infty$, we obtain $Y(t)\to 0$. Because the infection-related terms in the uninfected subsystem consequently vanish, the variation-of-constants formula gives $S(t)\to\Lambda/\mu$ and $R(t)\to 0$.

Both hypotheses hold, so $\mathcal{E}^0$ is globally asymptotically stable in Γ whenever $\mathcal{R}_0<1$. Biologically, once the reproduction number is pushed below unity, the infection is cleared irrespective of how large the initial outbreak was, and it cannot re-establish itself spontaneously under the assumption of the model. □

6. Elasticity (normalized sensitivity) analysis

Threshold conditions are only actionable once one knows which parameters move $\mathcal{R}_0$ appreciably. For a parameter p, the normalized forward sensitivity index, or elasticity, is

$$\Upsilon_p^{\mathcal{R}_0}=\frac{\partial\mathcal{R}_0}{\partial p}\cdot\frac{p}{\mathcal{R}_0},\tag{6.1}$$

which reports the percentage change in $\mathcal{R}_0$ produced by a one percent change in p. Because $\mathcal{R}_0$ is available in the closed form (4.4), every index can be differentiated analytically rather than estimated numerically:

$$\begin{aligned}
&\Upsilon_{\beta}^{\mathcal{R}_0} = 1, && \Upsilon_{\sigma}^{\mathcal{R}_0} = \frac{\mu+\varphi_E}{m_1}, && \Upsilon_{\varphi_E}^{\mathcal{R}_0} = -\frac{\varphi_E}{m_1},\\
&\Upsilon_{\gamma}^{\mathcal{R}_0} = -\frac{\gamma}{m_2}, && \Upsilon_{\varphi_I}^{\mathcal{R}_0} = -\frac{\varphi_I}{m_2}, && \Upsilon_{\theta}^{\mathcal{R}_0} = -\frac{\theta}{m_2},\\
&\Upsilon_{\delta_I}^{\mathcal{R}_0} = -\frac{\delta_I}{m_2}, && \Upsilon_{\mu}^{\mathcal{R}_0} = -\mu\Big(\frac{1}{m_1}+\frac{1}{m_2}\Big), && \Upsilon_{\Lambda}^{\mathcal{R}_0} = \Upsilon_{\omega}^{\mathcal{R}_0} = \Upsilon_{\psi}^{\mathcal{R}_0} = \Upsilon_{\delta_T}^{\mathcal{R}_0} = \Upsilon_{\delta_Q}^{\mathcal{R}_0} = 0.
\end{aligned} \tag{6.2}$$

Table 2 evaluates (6.2) at the baseline calibration, and Figure 2 displays the same information; bars above and below the axis indicate parameters that amplify and suppress transmission, respectively.

Table 2. Normalized sensitivity indices of $\mathcal{R}_0$ at the baseline parameter set of Table 1. Closed forms follow from (4.4).

Parameter	Role	Closed form	Index
β	Transmission coefficient	1	+1.0000
σ	Latency → infectiousness	$(\mu+\varphi_E)/m_1$	+0.3372
φ_I	Isolation of infectious cattle	$-\varphi_I/m_2$	−0.5262
γ	Natural recovery	$-\gamma/m_2$	−0.3947
φ_E	Quarantine of exposed cattle	$-\varphi_E/m_1$	−0.3370
μ	Natural mortality	$-\mu(1/m_1+1/m_2)$	−0.0003
θ	Treatment uptake	$-\theta/m_2$	−0.0395
δ_I	Disease-induced mortality in I	$-\delta_I/m_2$	−0.0395
Λ, ω, ψ, δ_T, δ_Q	Absent from $\mathcal{R}_0$	0	0.0000

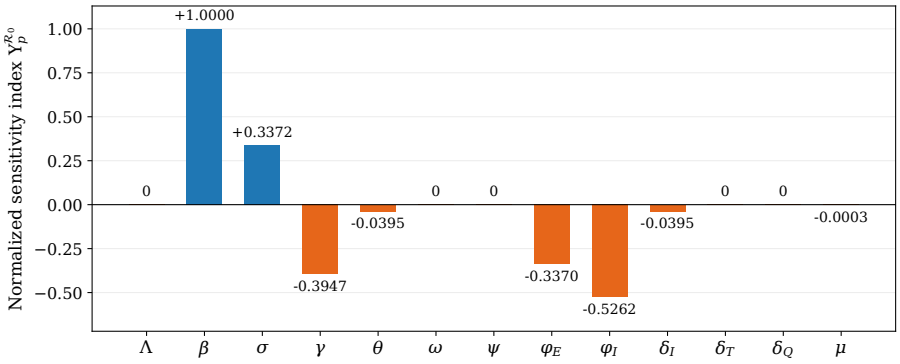

Figure 2. Normalized sensitivity indices of $\mathcal{R}_0$ with respect to each model parameter, evaluated at the baseline calibration.

Four features of Table 2 deserve comment.

Transmission dominates. The elasticity of β is exactly +1, an algebraic consequence of the linear appearance of β in (4.4): Halving effective contact halves $\mathcal{R}_0$. Vector control, restriction of animal movement, farm-level biosecurity, and prompt removal of clinical cases all act on this single coefficient and are therefore the highest-yield interventions.

Isolation of infectious cattle is the strongest suppressor. With $\Upsilon_{\varphi_I}^{\mathcal{R}_0} = -0.5262$, φ_I ranks second in absolute magnitude behind β. Its efficiency has a simple explanation: Infectious animals are the only

source of new infections, so shortening their infectious window removes transmission opportunities rather than merely redistributing them.

Quarantine of exposed cattle. The index $\Upsilon_{\varphi_E}^{\mathcal{R}_0} = -0.3370$ shows that intercepting animals during latency also lowers $\mathcal{R}_0$ substantially by reducing the fraction of exposed animals that ever reach the infectious class. The two indices together quantify what the SEIQTR structure was built to expose: The two arms of a quarantine program act on different factors of $\mathcal{R}_0$, and their effects compound. In an SEITR framework without an explicit Q class, this decomposition is unavailable, and the relative value of surveillance-driven early quarantine against clinical-case isolation cannot be assessed.

Recovery and treatment. Natural recovery has a sizeable negative index (-0.3947), so improved husbandry, supportive care, and prompt clinical management shorten the infectious period and depress $\mathcal{R}_0$. Treatment uptake θ and disease-induced mortality δ_I both act only through m_2, and both register -0.0395 at baseline; the small magnitude reflects their small baseline values rather than any structural weakness of treatment. The parameters Λ, ω, ψ, δ_T, and δ_Q do not appear in (4.4) and thus have zero elasticity, although they do shape the transient dynamics and the endemic level through (4.6).

6.1. Joint parameter effects

Elasticities are local, one-parameter measures. To see how pairs of parameters interact, $\mathcal{R}_0$ is plotted as a surface in Figure 3 and as a contour map in Figure 4 over the same grids.

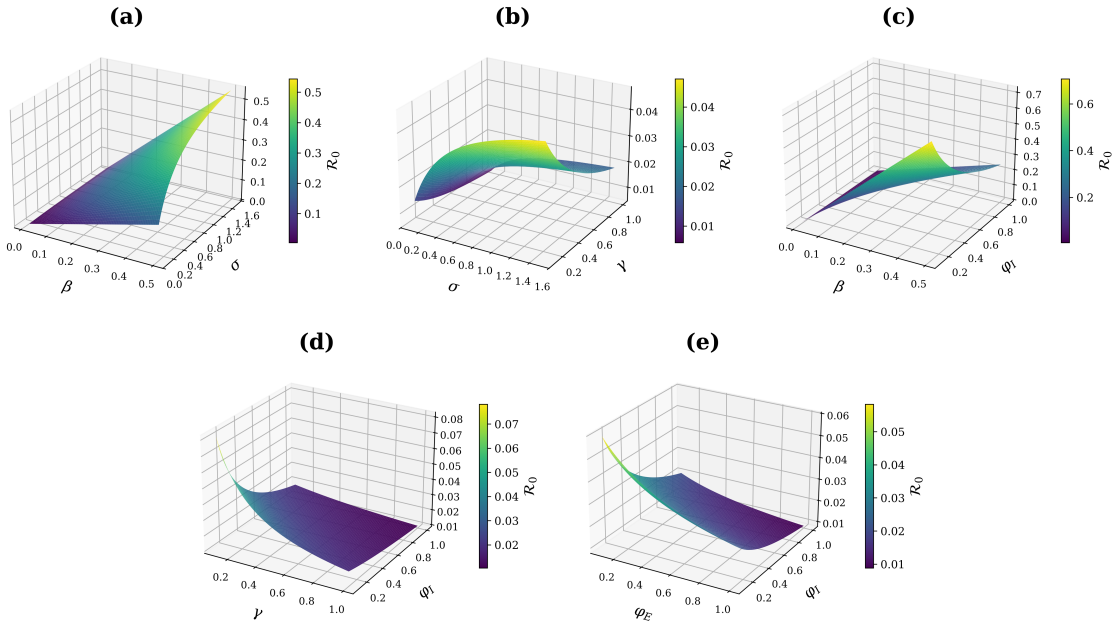

Figure 3. Response surfaces of $\mathcal{R}_0$: (a) β and σ; (b) σ and γ; (c) β and φ_I; (d) γ and φ_I; (e) φ_E and φ_I. All remaining parameters are held at their revised baseline values.

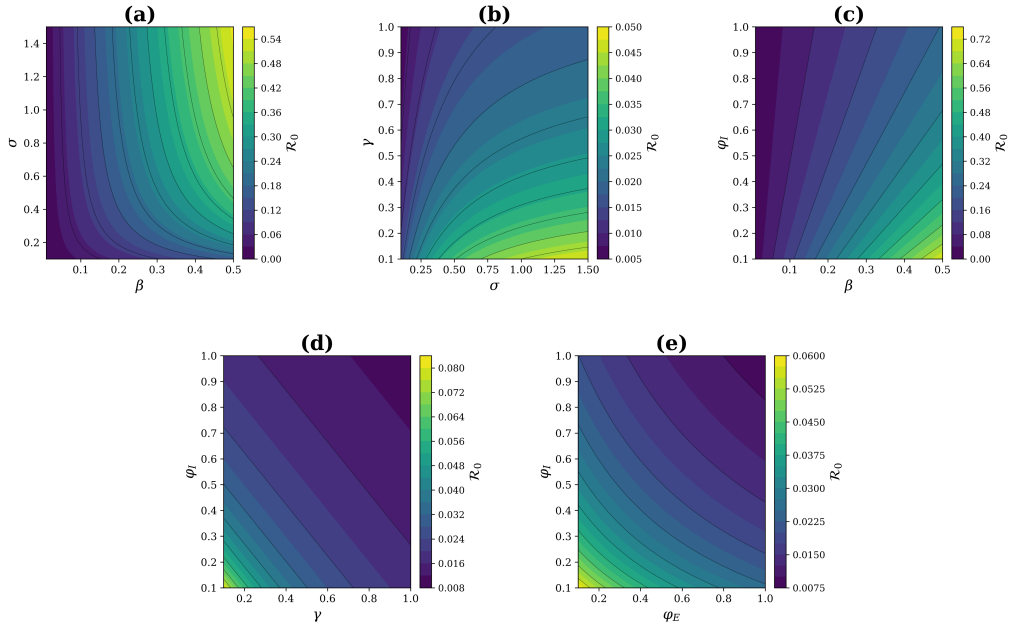

Figure 4. Contour maps of $\mathcal{R}_0$: (a) β and σ; (b) σ and γ; (c) β and φ_I; (d) γ and φ_I; (e) φ_E and φ_I. All remaining parameters are held at their revised baseline values.

Panels (a) show $\mathcal{R}_0$ against β and σ. The surface rises monotonically in both directions and is steepest along β, with the largest values confined to the upper-right corner, where fast progression through latency is combined with high contact intensity. Panels (b) contrast σ with γ: The surface decreases as γ grows, indicating that accelerating recovery reduces the reproduction number, whereas increasing the progression rate has the opposite effect. Panels (c) combine β with φ_I and make the compensating role of isolation explicit; an increase in φ_I can offset a substantial rise in β, which is exactly the situation faced during a vector-abundant season. Panels (d) pair γ with φ_I; the response surface and contour lines show that increasing either natural recovery or isolation reduces $\mathcal{R}_0$. Their combined influence further suppresses disease transmission. Panels (e) show the two quarantine parameters together: The contours demonstrate that increasing either φ_E or φ_I reduces $\mathcal{R}_0$, with the influence of φ_I being stronger at the considered baseline. The joint reduction is nonlinear. This is the graphical counterpart of $|\Upsilon_{\varphi_I}^{\mathcal{R}_0}| > |\Upsilon_{\varphi_E}^{\mathcal{R}_0}|$.

6.2. Robustness analysis of assumed parameter values

To assess the robustness of the model predictions with respect to the assumed parameter values, a Monte Carlo analysis was performed using 20,000 independently generated parameter combinations. The parameters ψ, φ_E, φ_I, and δ_Q were sampled independently from uniform distributions within ±50% of their baseline values, whereas all other parameters remained fixed. This analysis was intended to examine the stability of the reproduction threshold and the sensitivity ranking under variations in the assumed rates.

The calculated values of $\mathcal{R}_0$ ranged from 0.018974 to 0.045216, with a mean of 0.028830. All sampled parameter combinations satisfied $\mathcal{R}_0 < 1$, indicating that the disease-free equilibrium remained globally asymptotically stable throughout the considered parameter ranges, in accordance with Theorem 5.3. Thus, the threshold conclusion is not sensitive to these variations around the selected

baseline calibration.

The sensitivity analysis further showed that the absolute elasticity associated with infectious cattle isolation exceeded that of exposed cattle quarantine in 96.26% of the sampled combinations. However, isolation exceeded natural recovery in 75.12% of the combinations, indicating that the relative ranking of these interventions is not uniform across the sampled parameter space. Overall, the results support the robustness of the disease-free threshold while highlighting the dependence of intervention priorities on the assumed parameter values.

7. Deep neural network approximation

System (2.2)–(2.7) is nonlinear and coupled, and no closed-form trajectory is available. The analyses of the previous sections require the solution to be recomputed for many parameter combinations, which is precisely the setting in which a trained surrogate pays for itself: Once fitted, a network returns the state at any time by a single forward pass without stepping through a mesh. This section describes the construction of such a surrogate.

7.1. Reference data and preprocessing

Compactly, the model is

$$\frac{\mathrm{d}\boldsymbol{Y}}{\mathrm{d}t} = \boldsymbol{f}(\boldsymbol{Y}, \boldsymbol{\Theta}), \qquad \boldsymbol{Y}(t) = (S, E, I, Q, T, R)^{\top}, \tag{7.1}$$

where $\boldsymbol{\Theta}$ collects the epidemiological parameters. Reference trajectories are produced with the classical explicit fourth-order Runge–Kutta scheme on $t \in [0, 200]$ with step size $h = 0.1$, starting from

$$(S_0, E_0, I_0, Q_0, T_0, R_0) = (5000,\ 800,\ 600,\ 400,\ 200,\ 0) \tag{7.2}$$

and with $\boldsymbol{\Theta}$ fixed at the baseline values of Table 1. These synthetic trajectories stand in for field observations, which for LSD outbreaks are rarely available at compartment resolution.

Inputs and outputs are rescaled before training, which conditions the optimization and prevents the large susceptible counts from dominating the loss. Time is mapped onto the unit interval, and each compartment is normalized using the minimum and maximum values obtained from the training data:

$$\hat{t} = \frac{t}{t_f}, \qquad \widehat{Y}_i = \frac{Y_i - Y_{i,\min}^{\text{train}}}{Y_{i,\max}^{\text{train}} - Y_{i,\min}^{\text{train}}}, \qquad i = 1, \ldots, 6. \tag{7.3}$$

The baseline RK4 trajectory is divided into five time intervals, with observations randomly allocated to training (70%), validation (15%), and testing (15%) sets within each interval. The validation set is used for model selection, and the held-out test set is used to evaluate predictive accuracy.

7.2. Network architecture

A fully connected feed-forward network is used. It takes the scaled time $\hat{t}$ as its single input and returns the six scaled compartments simultaneously so that one network represents the entire state trajectory. A layer with weight matrix $\boldsymbol{W}^{(\ell)}$ and bias $\boldsymbol{b}^{(\ell)}$ acts as

$$\boldsymbol{a}^{(\ell)} = \varsigma(\boldsymbol{W}^{(\ell)}\boldsymbol{a}^{(\ell-1)} + \boldsymbol{b}^{(\ell)}), \qquad \varsigma(x) = \begin{cases} x, & x \geq 0, \\ \alpha x, & x < 0, \end{cases} \tag{7.4}$$

with ς the LeakyReLU activation ($\alpha = 0.01$). The retained architecture, selected as described below, has three hidden layers of 128 units each with LeakyReLU activation functions followed by a linear output layer of six units. No dropout regularization is applied in the final configuration, as supported by the comparative results presented in Section 7.4 and Table 3. The network architecture is illustrated in Figure 5.

Table 3. Effect of the dropout rate on surrogate accuracy: Relative L^2 error per compartment on the validation set, and the mean coefficient of determination. All other settings are those of Table 4.

Dropout	S	E	I	Q	T	R	Mean R^2
0	0.000016	0.050852	0.054780	0.006030	0.002106	0.001361	0.999011
0.1	0.000051	0.153771	0.071147	0.061509	0.028034	0.001908	0.994225
0.2	0.000080	0.250902	0.161246	0.081415	0.035020	0.004904	0.983034
0.5	0.000258	0.607016	0.469987	0.141334	0.078478	0.020474	0.886919

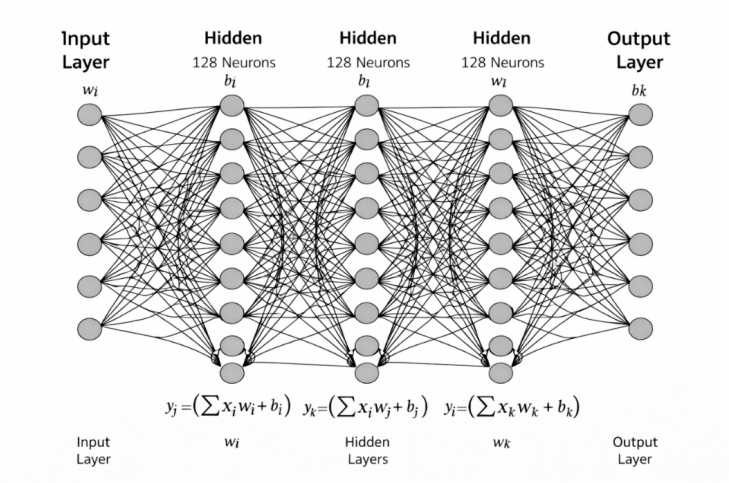

Figure 5. Architecture of the feed-forward network: One input node ($\hat{t}$), three hidden layers of 128 neurons, and six output nodes, one per compartment.

7.3. Hyperparameter selection

Depth, width, activation, optimizer, and loss were chosen by a grid search over the candidate sets listed in Table 4, with each configuration trained under identical conditions and ranked by its validation loss history. Figure 6 reports the comparison. LeakyReLU converged fastest and most smoothly among the activations, with sigmoid stagnating at a markedly higher loss; Adam dominated SGD, Adagrad, and Adamax by roughly an order of magnitude in final loss; and the Huber loss was retained over the mean squared error (MSE) and root mean square error (RMSE) for its reduced sensitivity to the large initial residuals produced by the rapidly decaying compartments.

Table 4. Hyperparameter configuration of the optimized network.

Hyperparameter	Candidates evaluated	Retained
Hidden layers	Grid search over depth	3
Neurons per hidden layer	Grid search over width	128
Output neurons	—	6 (one per compartment)
Activation	ReLU, LeakyReLU, Tanh, Sigmoid, SeLU	LeakyReLU
Optimizer	Adam, SGD, Adagrad, Adamax	Adam
Loss	MSE, Huber, RMSE	Huber
Dropout rate	0, 0.1, 0.2, 0.5 after each hidden layer (Sec. 7.4)	0
Data partition (train/validation/test)	—	70%/15%/15% (train/val/test)
Training epochs	—	1000
Learning rate (Adam)	—	10^{-3}
Mini-batch size	—	64
Huber threshold c	—	1.0 (on scaled output)
Reference solver	RK4, $h = 0.1$, $t \in [0, 200]$	—
Implementation	—	`code/train_dnn.py`

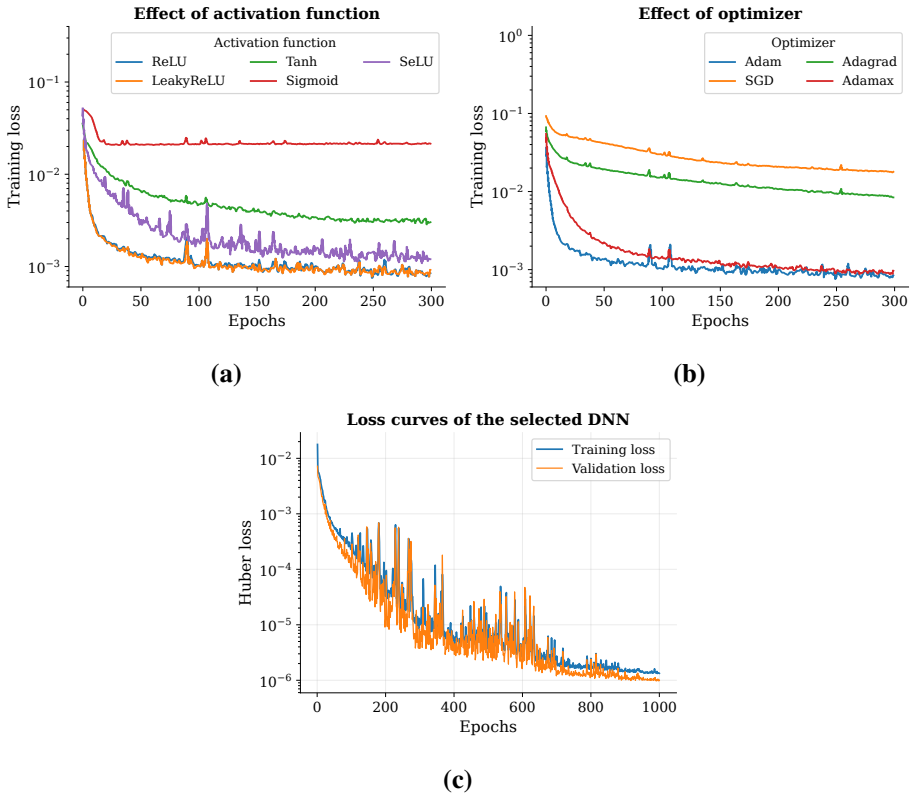

Figure 6. Training-loss histories used for hyperparameter selection: (a) activation functions, (b) optimization algorithms, (c) training and validation loss curves of the selected DNN configuration.

7.4. Effect of dropout

Dropout is a standard remedy for overfitting, and adaptive dropout schemes have recently been designed for complex feature-learning tasks [77]; however, its usefulness depends on the task. Here,

the network has a single scalar input and must interpolate six smooth, rapidly varying curves; there is no input noise to average over, and randomly deleting half of the units destroys precisely the fine structure the network is being asked to represent. Table 3 quantifies this by retraining the identical architecture at four dropout rates and comparing the relative L^2 error on the validation set. Accuracy degrades monotonically with the dropout rate across the considered configurations, with the exposed class exhibiting a substantial increase in relative error from 5.0852×10^{-2} to 6.0702×10^{-1}. Regularization is therefore not retained in the final configuration; the training and validation losses exhibit broadly consistent convergence without sustained divergence, suggesting that substantial overfitting is not evident.

7.5. Training

Let y denote a reference value produced by RK4 and $\hat{y}$ the corresponding network output. Training minimizes the Huber loss

$$\mathcal{L}(y, \hat{y}) = \begin{cases} \dfrac{1}{2}(y - \hat{y})^2, & |y - \hat{y}| \le c, \\ c\Big(|y - \hat{y}| - \dfrac{1}{2}c\Big), & |y - \hat{y}| > c, \end{cases} \tag{7.5}$$

which is quadratic for small residuals and linear for large ones, with the threshold c marking the transition. Weights and biases are updated by backpropagation using the Adam optimizer, with early stopping applied when the validation loss fails to improve for 100 consecutive epochs. The network parameters corresponding to the lowest validation loss are retained. The complete procedure is summarized in Algorithm 1. The predictive performance of the trained network was evaluated using the mean absolute error (MAE), RMSE, relative L^2 error, and coefficient of determination (R^2), calculated separately for each compartment against the RK4 reference solutions.

Algorithm 1. Training of the SEIQTR surrogate network.

Input: Parameter vector $\boldsymbol{\Theta}$, initial state (7.2), horizon $t_f = 200$, step $h = 0.1$, epoch budget N_e.
Output: Trained surrogate $\widehat{\boldsymbol{Y}}_{\boldsymbol{W}}(\hat{t})$.
Integrate (7.1) by RK4 to obtain reference pairs $\{(t_k, \boldsymbol{Y}_k)\}_{k=0}^{K}$;
Rescale inputs and outputs according to (7.3);
Split the scaled pairs into training (70%), validation (15%), and testing (15%) sets;
Initialize weights $\boldsymbol{W}$ and biases $\boldsymbol{b}$;
for $e \leftarrow 1$ **to** N_e **do**
  foreach *mini-batch of training pairs* **do**
    Forward pass through (7.4) to obtain $\widehat{\boldsymbol{Y}}$;
    Evaluate the Huber loss (7.5);
    Backpropagate and update $(\boldsymbol{W}, \boldsymbol{b})$ with Adam;
  end
  Evaluate the validation loss; retain $(\boldsymbol{W}, \boldsymbol{b})$ if it is the best so far;
  If the validation loss does not improve for 100 consecutive epochs, stop training;
end
Rescale the network output back to population units.

8. Numerical results

This section evaluates the trained surrogate against its RK4 reference and then uses the model to compare control scenarios. Throughout, parameters are held at the baseline of Table 1 except for the one being varied.

8.1. Surrogate accuracy

Figure 7 superimposes network predictions on RK4 trajectories for all six compartments over the full 200-day window. The curves show close agreement, and the network reproduces every qualitative feature of the dynamics: The initial decline and subsequent gradual increase of S, the rapid collapse of E and I, the transient peak of Q near $t \approx 2$ days fed by inflow from both E and I, the decline of T, and the rise of R to about 1721 animals at $t \approx 49$ days, followed by its slow decay as the inflows dry up, and natural mortality takes over. Quantitative errors are reported in Table 5: The coefficient of determination exceeds 0.998 in every compartment, and the relative L^2 error stays below 4×10^{-2}, with the largest value occurring for I, whose steep initial transient is the hardest feature to represent.

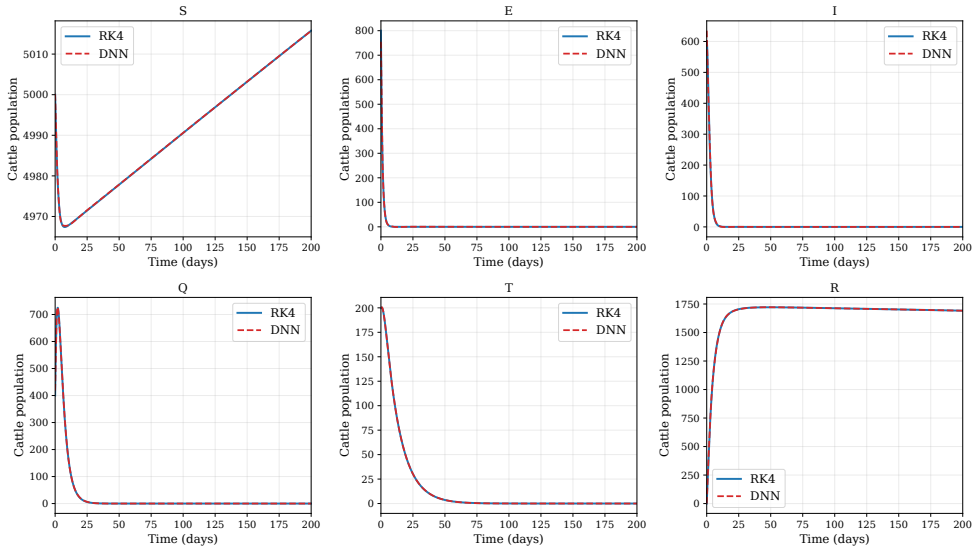

Figure 7. Neural-network predictions (dashed) against RK4 reference solutions (solid) for each compartment over $t \in [0, 200]$, at the baseline calibration of Table 1 and the initial conditions (7.2).

Table 5. Accuracy of the trained surrogate against the RK4 reference on the held-out test set, in population units. Network settings are those of Table 4.

Compartment	MAE	RMSE	Relative L^2 error	R^2
S	0.030573	0.063982	1.282×10^{-5}	0.999980
E	0.200181	0.885994	2.402×10^{-2}	0.999411
I	0.350875	1.903890	3.155×10^{-2}	0.998976
Q	0.244863	0.953502	7.220×10^{-3}	0.999945
T	0.042958	0.074645	1.731×10^{-3}	0.999997
R	0.552630	1.652659	9.872×10^{-4}	0.999936

The dynamics themselves are readily interpreted. The susceptible population initially decreases due to infection and natural mortality but gradually increases as infection declines and as recruitment exceeds the remaining losses. The exposed and infectious classes decrease rapidly during the early epidemic period without developing a sustained epidemic wave: At the baseline calibration, the incidence at $t = 0$, namely $\beta S_0 I_0/N_0 \approx 13.7$ animals per day, is substantially smaller than the outflow $m_1 E_0 = 712.10$ per day, so $\dot{E}(0) < 0$, consistent with the disease-free stability condition $\mathcal{R}_0 \approx 0.0279 < 1$. The quarantined class is the only infected compartment that grows, peaking at roughly 725 animals near $t \approx 2$ days, because it receives from two compartments at once before its own outflow takes over. Recovered animals accumulate while infection persists and decline afterwards, as with $\mathcal{R}_0 < 1$, no new inflow sustains the class.

8.2. Scenario analysis

A one-parameter-at-a-time study was carried out over the first 40 days, which covers the epidemic transient; the initial conditions (7.2) and all nonvaried parameters were held fixed.

Transmission coefficient. Figure 8 tracks E, I, and R as β ranges over 0.012, 0.128, 0.256, 0.512, and 0.7 day^{-1}. The exposed class responds most directly, as expected from its position immediately downstream of the incidence term. Larger β keeps both E and I elevated for longer, the smallest value producing the fastest decay and $\beta = 0.7$ the slowest. The recovered class also rises with β, but this must not be read as an improvement: More animals recover only because more animals were infected in the first place, so the higher R curve records a larger cumulative burden, paid for in lost production and in the disease-induced deaths that accompany it.

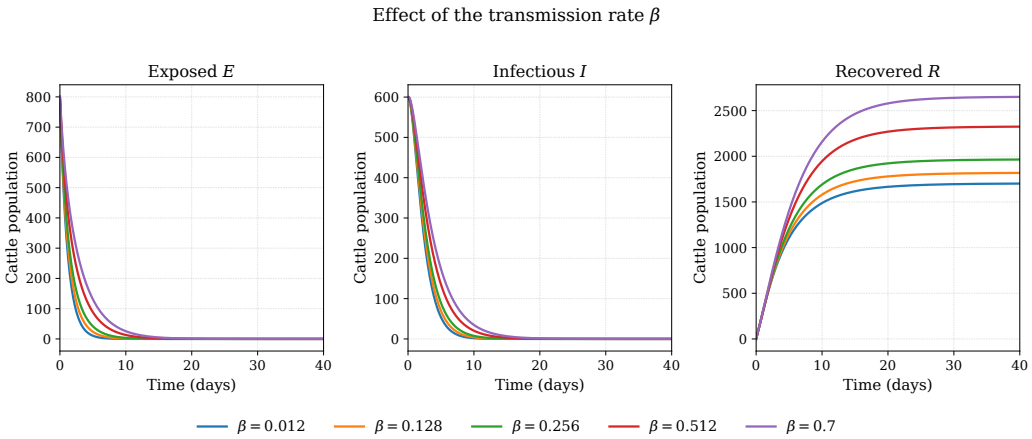

Figure 8. Effect of the transmission coefficient β on the exposed, infectious, and recovered classes.

Isolation of infectious cattle. Varying φ_I over 0.1, 0.3, 0.7, 1.3, and 2.0 day^{-1} gives Figure 9. The infectious class contracts sharply as φ_I grows, as the mean residence time in I is $1/m_2$, and φ_I enters m_2 additively. The quarantined class exhibits a substantially higher transient peak as the isolation rate increases, highlighting the need for adequate quarantine capacity during the early stages of an outbreak. Isolation is therefore highly effective at suppressing active infection, but its effectiveness is contingent on that capacity being available when the peak arrives.

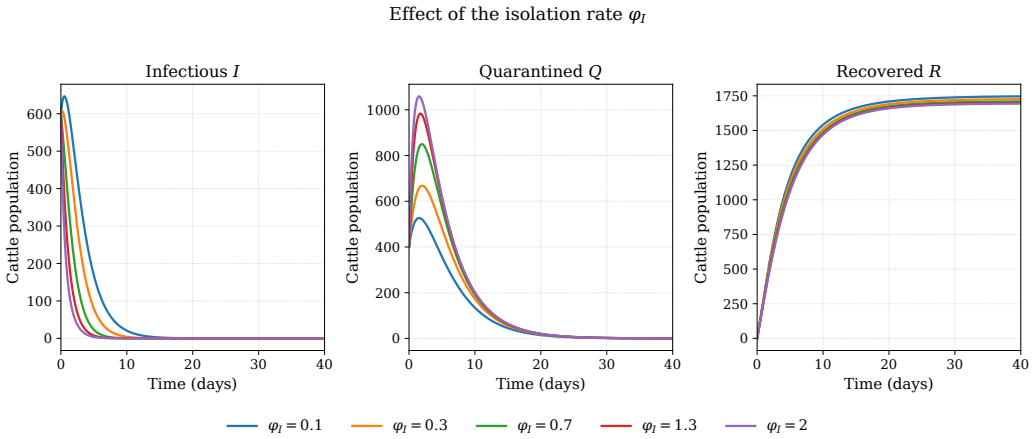

Figure 9. Effect of the isolation rate of infectious cattle on the infectious, quarantined, and recovered classes.

Quarantine of exposed cattle. Figure 10 varies φ_E over 0.1, 0.5, 0.9, 1.3, and 2.0 day^{-1}. The exposed class falls rapidly with increasing φ_E, and the infectious class follows because fewer latently infected animals ever reach I. The quarantine peak again occurs earlier and higher. The mechanism differs from the previous scenario in an operationally important way: Isolation acts after infectiousness has begun, whereas quarantine of exposed animals prevents the infectious period from occurring at all. However, it requires surveillance capable of detecting animals before clinical signs appear, which is the harder requirement in the field.

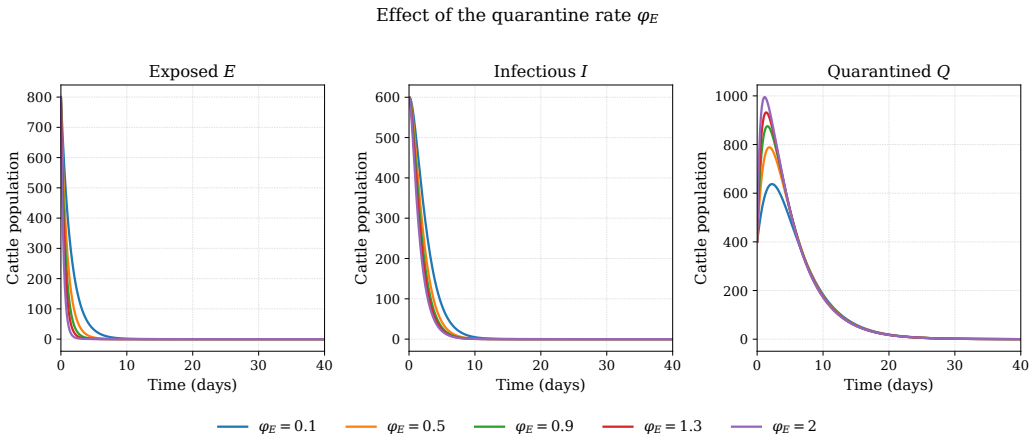

Figure 10. Effect of the quarantine rate of exposed cattle on the exposed, infectious, and quarantined classes.

8.3. Numerical verification of the reference solver

To further assess the numerical accuracy of the RK4 reference solutions and examine the feasibility of an alternative numerical approach, we compared the classical fourth-order Runge–Kutta (RK4) method with the forward Euler finite-difference method. Both methods were applied to the SEIQTR system using identical baseline parameters and initial conditions over the interval $t \in [0, 200]$. Three

step sizes, $h = 0.1$, 0.05, and 0.025, were considered for each method.

A fine-step RK4 solution with $h = 0.005$ was employed as the numerical reference. The MAE, RMSE, and maximum absolute error were calculated across all six compartments at common time points. The resulting errors are reported in Table 6.

Table 6. Numerical convergence comparison of the forward Euler finite-difference method and RK4.

Method	Step size h	MAE	RMSE	Maximum error
Forward Euler	0.100	0.218407	1.075583	13.220325
Forward Euler	0.050	0.108539	0.532332	6.483284
Forward Euler	0.025	0.054108	0.264846	3.211011
RK4	0.100	1.3471×10^{-6}	1.34029×10^{-5}	2.985893×10^{-4}
RK4	0.050	8.07×10^{-8}	8.011×10^{-7}	1.78277×10^{-5}
RK4	0.025	4.90×10^{-9}	4.89×10^{-8}	1.0875×10^{-6}

The results demonstrate consistent error reduction as the step size decreases. For the forward Euler method, halving the step size approximately halves the numerical errors, indicating first-order convergence. In contrast, the RK4 errors decrease by approximately a factor of sixteen, consistent with its fourth-order accuracy. The observed convergence orders, estimated from successive RMSE values, are approximately 1.01 for forward Euler and 4.05 for RK4, in close agreement with their respective theoretical orders.

Although both methods provide consistent approximations of the SEIQTR dynamics, RK4 achieves substantially smaller numerical errors at the considered step sizes. Therefore, RK4 is retained as the primary reference solver for evaluating the neural-network predictions. The comparison with the forward Euler method provides additional numerical evidence supporting the accuracy and reliability of the adopted reference solutions.

8.4. Validation under alternative initial conditions

To further assess the generalization capability of the neural-network approach, an additional experiment was conducted using multiple independently generated SEIQTR trajectories. A total of 60 initial-condition configurations were considered, with the initial population fixed at 7000 cattle and the epidemiological parameters held at their baseline values. The corresponding reference trajectories were generated using RK4 over $t \in [0, 200]$.

A separate initial-condition-conditioned DNN was constructed with time and the six initial compartment populations as inputs. The network consisted of three hidden layers with 128 neurons each and Tanh activation functions. The trajectories were divided into 40 training, 10 validation, and 10 independent testing scenarios, ensuring that the test trajectories were not used during training or model selection.

The network was trained using the Huber loss with an additional initial-condition penalty. Its predictive performance was evaluated on all 2001 time points of each independent test trajectory. The resulting errors are reported in Table 7.

Table 7. Prediction errors of the initial-condition-conditioned DNN on ten independent test trajectories.

Compartment	MAE	RMSE	Relative L^2 error	R^2
S	5.424439	8.127655	1.612×10^{-3}	0.999364
E	2.736625	7.260932	1.69683×10^{-1}	0.970878
I	1.461799	5.181104	1.06217×10^{-1}	0.988493
Q	1.800944	4.915939	4.4625×10^{-2}	0.997891
T	0.883998	1.382733	3.0574×10^{-2}	0.998944
R	6.939702	9.141290	5.464×10^{-3}	0.999214

The results indicate that the network can approximate trajectories corresponding to previously unseen initial conditions without scenario-specific retraining. The pooled coefficient of determination exceeds 0.97 across all six compartments, although the exposed and infectious classes exhibit comparatively larger relative errors. These findings provide additional evidence of generalization within the considered initial-condition configurations. Generalization with respect to the epidemiological parameters is examined separately in Section 8.5.

8.5. Validation under alternative parameter configurations

To assess whether the neural approach generalizes across epidemiological parameter values, a second conditional network was constructed that receives the time and the three control-relevant parameters $(\beta, \varphi_E, \varphi_I)$ as inputs and returns all six compartments. Sixty parameter vectors were drawn by Latin hypercube sampling over the ranges used in the scenario study of Section 8, namely $\beta \in [0.012, 0.7]$ day^{-1} and $\varphi_E, \varphi_I \in [0.1, 2.0]$ day^{-1}, with all remaining parameters at baseline and the initial conditions (7.2). For each vector, the RK4 reference trajectory was computed on $t \in [0, 200]$ with $h = 0.1$. The parameter vectors were partitioned into 40 training, 10 validation, and 10 independent test scenarios; the test parameter combinations were never used during training or model selection.

The network has three hidden layers of 128 Tanh units and receives the time, scaled both linearly and logarithmically to resolve the rapid early transient, together with the three parameters rescaled to $[0, 1]$. Outputs were min–max scaled using the training data. Training used Adam (learning rate 10^{-3}, mini-batch size 64) with a mean-squared-error loss and early stopping on the validation scenarios (patience 40 epochs); the weights with the lowest validation loss were retained. The errors over all 2001 time points of the ten unseen test scenarios are reported in Table 8.

Table 8. Prediction errors of the parameter-conditioned network on ten independent test scenarios with unseen values of $(\beta, \varphi_E, \varphi_I)$.

Compartment	MAE	RMSE	Relative L^2 error	R^2
S	2.4346	2.9428	5.983×10^{-4}	0.998182
E	1.3224	2.2242	5.849×10^{-2}	0.996551
I	1.5762	2.5480	8.248×10^{-2}	0.993135
Q	3.8851	4.6301	2.826×10^{-2}	0.999158
T	0.4012	0.4989	1.346×10^{-2}	0.999794
R	5.6268	7.8064	4.498×10^{-3}	0.998513

The coefficient of determination exceeds 0.993 in every compartment, and the relative L^2 error remains below 8.3×10^{-2}, the largest errors again occurring for the exposed and infectious classes, whose early decay rate depends most strongly on φ_E and φ_I. The network therefore reproduces the SEIQTR dynamics for parameter combinations that were not seen during training without scenario-specific retraining. It should be noted that all sampled combinations satisfy $\mathcal{R}_0 < 1$ (the test scenarios span $0.015 \leq \mathcal{R}_0 \leq 0.168$) because the scenario range of β lies below the critical value $\beta^\star$; generalization to the endemic regime $\mathcal{R}_0 > 1$ and to parameters outside the sampled ranges is not claimed. The script reproducing this experiment is provided with the supplementary material.

9. Discussion

Mathematical work on LSD has grown quickly, encompassing reviews, integer-order and SEIR-type models (Section 1). Fractional-order models of LSD have also been developed [74]. Optimal control through pharmaceutical interventions has been analyzed as well [75]. However, the available models describe removal from the transmission chain as a single process. The model developed here separates it into quarantine of latently infected animals and isolation of infectious animals, and the analysis shows that the distinction is not cosmetic: The two rates enter different factors of $\mathcal{R}_0$ in (4.4), carry different elasticities, and place different demands on surveillance and holding capacity.

The suggested studies provide useful methodological context for the present investigation. The crossover fractional LSD model considered by Sweilam et al. [35] explores alternative representations of disease dynamics, whereas the present SEIQTR formulation focuses on distinguishing the removal of exposed and infectious cattle through separate quarantine and isolation pathways. Similarly, the numerical schemes of Abou Hasan et al. [36] address the computational treatment of fractional systems. Their later discretization scheme [37] extends this treatment to time-delay systems. Although these formulations differ from the integer-order ODE system considered here, they emphasize the importance of numerical accuracy and reliable discretization. In this regard, the comparison between forward Euler and RK4 presented in Section 8.3 provides an additional assessment of the numerical reliability of the reference solutions used to train and evaluate the proposed neural-network surrogate.

Analytically, the model is well-posed on the compact invariant region (3.3); its disease-free state is locally and globally asymptotically stable below the threshold (Theorems 5.1 and 5.3); and its endemic state exists, is unique, and is biologically admissible exactly above it (Proposition 4.2). Because I^* increases continuously from zero as $\mathcal{R}_0$ crosses one, the transition is a forward bifurcation, and driving $\mathcal{R}_0$ below unity is both necessary and sufficient for elimination—there is no subcritical endemic branch that would make control harder than the threshold suggests.

Numerically, the elasticity ranking $|\Upsilon_\beta| > |\Upsilon_{\varphi_I}| > |\Upsilon_\gamma| > |\Upsilon_{\varphi_E}|$ and the scenario simulations point the same way, and Remark 4.1 turns the ranking into figures a veterinary service can use: At the baseline calibration, the combined quarantine effort accounts for a 68.6% reduction in $\mathcal{R}_0$, and the critical isolation effort needed to contain an outbreak with $\beta = 2$ day^{-1} is about 0.966 day^{-1}. The additional numerical comparison also confirms the expected first-order convergence of forward Euler and fourth-order convergence of RK4, supporting the selection of RK4 as the reference solver for the neural surrogate.

The neural surrogate is the computational counterpart of this analysis. Trained on RK4 trajectories, it reproduces all six compartments with $R^2 > 0.998$ throughout (Table 5) and returns the state at any

instant in a single forward pass, which is attractive when the model must be evaluated repeatedly. It should be read as an interpolant of the dynamics, not as an independent solver: It was fitted to one parameter vector and one set of initial conditions, and its guarantees do not extend beyond them. The additional multitrajectory experiments extend the assessment to unseen initial conditions (Section 8.4) and to unseen combinations of β, φ_E and φ_I (Section 8.5) using separately trained conditional networks, with $R^2 > 0.97$ and $R^2 > 0.993$, respectively. Nevertheless, predictive accuracy varies between scenarios; both experiments are confined to the subthreshold regime and to the sampled ranges; and generalization to the endemic regime, to the remaining parameters, or to field observations has not been established.

The practical significance of the proposed framework lies in its potential to support veterinary planning by identifying the relative importance of quarantine and isolation at different stages of infection. The findings may help assess intervention priorities, anticipate quarantine capacity requirements, and inform early disease-control strategies. However, the quantitative predictions depend on the assumed parameter values and simplified transmission dynamics. Therefore, the results should be interpreted within the considered modeling assumptions, and further calibration and validation using field data are required before their application to real-world LSD control programs.

9.1. Limitations and directions for further work

Several limitations should be stated plainly.

(1) *Parameter provenance.* Four parameters, namely ψ, φ_E, φ_I, and δ_Q, were assigned illustrative baseline values as part of the modeling assumptions, and the recruitment rate Λ was derived from the baseline population and natural mortality rate. The elasticities in Table 2 are local and depend on the point at which they are evaluated, so the ranking should be re-examined once field estimates are available. Formal identifiability analysis and Bayesian calibration against outbreak records are natural next steps.

(2) *Baseline regime.* At the baseline calibration, $\mathcal{R}_0 \approx 0.0279$, which is well below unity, so every simulation reported here converges to the disease-free state, and the trajectories describe the clearance of an existing outbreak rather than an emerging epidemic. Endemic behavior requires $\beta > \beta^\star \approx 1.14679$ day^{-1} at fixed remaining parameters; a complementary study in that regime would exercise Proposition 4.2 directly.

(3) *Vector dynamics.* LSDV is spread mechanically by arthropod vectors, whose abundance is strongly seasonal. The present formulation absorbs this into a constant β. An explicit vector compartment or a periodic $\beta(t)$ would capture seasonality and allow a seasonal reproduction number to be computed.

(4) *Absent interventions.* Vaccination, the mainstay of LSD control in endemic settings, and waning immunity are not represented. Nor is the cost of quarantine: Because φ_E and φ_I are competing uses of the same budget, an optimal-control formulation with a cost functional would identify the efficient allocation between them rather than merely ranking them.

(5) *Scope of the surrogate.* A physics-informed formulation, in which the residual of (2.2)–(2.7) enters the loss, and the parameters are supplied as additional inputs, could provide a surrogate that generalizes over all model parameters, including the endemic regime $\mathcal{R}_0 > 1$ not covered by the experiments of Sections 8.4 and 8.5, and remove the dependence on precomputed reference

trajectories.

9.2. Future research directions

Building on the present framework, several extensions are planned. First, the constant parameters will be replaced by time-varying ones—for instance, a seasonal transmission rate $\beta(t)$ and time-dependent control efforts $\varphi_E(t)$ and $\varphi_I(t)$. Robust zeroing-neural-network solvers designed for time-varying problems [51] will be explored for tracking the resulting dynamics. Fuzzy-parameter variants [52] may further help in estimating parameters from data. Second, the SEIQTR model can be embedded in an early-warning and decision-support pipeline, analogous to proactive warning systems proposed for monkeypox [69], in which surveillance records trigger updated forecasts of $\mathcal{R}_0$ and of quarantine capacity requirements. Third, the mechanistic model could be coupled with deep-learning detection of LSD lesions in cattle [65], so that automatically detected cases inform the isolation rate φ_I in near-real time. Drone-based monitoring [71] could support such case detection at the herd level. Fourth, uncertainty in the surrogate could be quantified by ensemble learning [70], providing confidence bands for the predicted trajectories. Adaptive regularization [77] could further improve the robustness of the trained network. Finally, a fractional-order formulation of the SEIQTR system could be solved with the improved schemes of Abou Hasan et al. [36]. A delay formulation could use the corresponding time-delay discretization [37]. An optimal-control problem that allocates resources between quarantine and isolation is another natural next step.

10. Conclusions

An SEIQTR model for lumpy skin disease has been formulated in which the quarantine of exposed cattle and the isolation of infectious cattle are governed by separate rates alongside treatment and recovery. The model was shown to be well-posed, with unique, non-negative, and bounded solutions confined to a compact invariant region. Both equilibria were obtained—the endemic one in a compact, closed form parameterized by a single scalar—and the disease-free state was proved locally and globally asymptotically stable for $\mathcal{R}_0 < 1$, with the endemic state existing and unique exactly when $\mathcal{R}_0 > 1$.

Analytical elasticity indices identified the transmission coefficient as the strongest positive contributor to $\mathcal{R}_0$, with unit elasticity. At the baseline calibration, the isolation of infectious cattle (-0.5262), natural recovery (-0.3947), and quarantine of exposed cattle (-0.3370) were identified as the principal factors reducing $\mathcal{R}_0$, in decreasing order of influence. At the baseline calibration, the combined quarantine effort lowers $\mathcal{R}_0$ by some 68.6%. Surface and contour diagnostics confirmed that transmission and progression amplify outbreak potential jointly, whereas recovery and the two quarantine rates suppress it, and the scenario study reproduced the same ordering in the time domain while quantifying the quarantine capacity that an aggressive isolation policy requires.

An optimized feed-forward network trained on fourth-order Runge–Kutta trajectories reproduced all six compartments over the simulation horizon with $R^2 > 0.998$ and relative L^2 errors below 3.2×10^{-2} on the held-out test set (Table 5), and the initial-condition-conditioned network attained $R^2 > 0.97$ on ten unseen trajectories (Table 7), and the parameter-conditioned network attained $R^2 > 0.993$ on ten unseen parameter combinations (Table 8), supporting its use as an inexpensive surrogate for repeated evaluation under comparable settings. Taken together, the analytical, sensitivity, numerical,

and learning-based components form a single framework for assessing quarantine-based control of LSD and provide a basis for extensions towards optimal control, seasonal transmission, and calibration against outbreak data.

Data availability

Synthetic numerical data were generated from the SEIQTR model using the RK4 method. All simulations are reproducible from the governing equations, the parameter values in Table 1, and the initial conditions in (7.2). The computational scripts used to generate the figures and train the neural networks are provided as supplementary material.

Author contributions

Rubiqa Zulfiqar: Conceptualization, mathematical analysis, numerical computation and verification, writing of the original draft; Abdul Mannan: Computation, validation, review and editing; Muhammad Farhan Hanif and Ebraheem Alzahrani: Supervision, symbolic and graphical computation, review and editing. All authors have read and approved the final version of the manuscript for publication.

Use of Generative-AI tools declaration

The authors used ChatGPT (OpenAI) only for grammar checking and language editing of the manuscript. The authors reviewed all edits and take full responsibility for the content of this article.

Acknowledgments

This project was funded by KAU Endowment (WAQF) at King Abdulaziz University, Jeddah, Saudi Arabia. The authors, therefore, acknowledge with thanks WAQF and the Deanship of Scientific Research (DSR) for technical and financial support.

Conflict of interest

The authors declare no conflicts of interest in this paper.

References

1. S. Babiuk, T. R. Bowden, D. B. Boyle, D. B. Wallace, R. P. Kitching, Capripoxviruses: an emerging worldwide threat to sheep, goats and cattle, *Transbound. Emerg. Dis.*, **55** (2008), 263–272. https://doi.org/10.1111/j.1865-1682.2008.01043.x
2. C. J. McInnes, I. K. Damon, G. L. Smith, G. McFadden, S. N. Isaacs, R. L. Roper, et al., ICTV virus taxonomy profile: Poxviridae 2023, *J. Gen. Virol.*, **104** (2023), 001849. https://doi.org/10.1099/jgv.0.001849

3. F. Namazi, A. K. Tafti, Lumpy skin disease, an emerging transboundary viral disease: a review, *Vet. Med. Sci.*, **7** (2021), 888–896. https://doi.org/10.1002/vms3.434

4. E. S. M. Tuppurainen, E. H. Venter, J. L. Shisler, G. Gari, G. A. Mekonnen, N. Juleff, et al., Review: capripoxvirus diseases: current status and opportunities for control, *Transbound. Emerg. Dis.*, **64** (2017), 729–745. https://doi.org/10.1111/tbed.12444

5. C. M. Chihota, L. F. Rennie, R. P. Kitching, P. S. Mellor, Attempted mechanical transmission of lumpy skin disease virus by biting insects, *Med. Vet. Entomol.*, **17** (2003), 294–300. https://doi.org/10.1046/j.1365-2915.2003.00445.x

6. B. Kaur, S. S. Dhillon, A. S. Pannu, C. S. Mukhopadhyay, Lumpy skin disease: a systematic review of mode of transmission, risk of emergence, and risk entry pathways, *Virus Genes*, **61** (2025), 1–8. https://doi.org/10.1007/s11262-024-02117-z

7. J. C. Lubinga, E. S. M. Tuppurainen, W. H. Stoltsz, K. Ebersohn, J. A. W. Coetzer, E. H. Venter, Detection of lumpy skin disease virus in saliva of ticks fed on lumpy skin disease virus-infected cattle, *Exp. Appl. Acarol.*, **61** (2013), 129–138. https://doi.org/10.1007/s10493-013-9679-5

8. *Food and Agriculture Organization of the United Nations, FAOSTAT statistical database*, FAO, 2018. Available from: `https://www.fao.org/faostat/en/`.

9. Z. Abera, H. Degefu, G. Gari, Z. Ayana, Review on epidemiology and economic importance of lumpy skin disease, *Int. J. Basic Appl. Virol.*, **4** (2015), 8–21.

10. B. Molina-Flores, P. Manzano-Baena, M. D. Coulibaly, *The role of livestock in food security, poverty reduction and wealth creation in West Africa*, Accra: FAO, 2020. https://doi.org/10.4060/ca8385en

11. R. G. Alders, A. Campbell, R. Costa, E. F. Guèye, M. A. Hoque, R. P. Garza, et al., Livestock across the world: diverse animal species with complex roles in human societies and ecosystem services, *Anim. Front.*, **11** (2021), 20–29. https://doi.org/10.1093/af/vfab047

12. M. H. Tageldin, D. B. Wallace, G. H. Gerdes, J. F. Putterill, R. R. Greyling, M. N. Phosiwa, Lumpy skin disease of cattle: an emerging problem in the Sultanate of Oman, *Trop. Anim. Health Prod.*, **46** (2014), 241–246. https://doi.org/10.1007/s11250-013-0483-3

13. H. Rgbe, *Lumpy skin disease (LSD): outbreak investigation, isolation and molecular detection in selected areas of east Shewa Zone, Ethiopia*, Addis Ababa: Addis Ababa University, 2012. Available from: `https://etd.aau.edu.et/handle/123456789/8791`.

14. H. J. Eom, E. S. Lee, H. S. Yoo, Lumpy skin disease as an emerging infectious disease, *J. Vet. Sci.*, **24** (2023), e42. https://doi.org/10.4142/jvs.23016

15. E. Renald, J. Buza, J. M. Tchuenche, V. G. Masanja, The role of modeling in the epidemiology and control of lumpy skin disease: a systematic review, *Bull. Natl. Res. Cent.*, **47** (2023), 141. https://doi.org/10.1186/s42269-023-01111-z

16. A. I. K. Butt, H. Aftab, M. Imran, T. Ismaeel, Mathematical study of lumpy skin disease with optimal control analysis through vaccination, *Alex. Eng. J.*, **72** (2023), 247–259. https://doi.org/10.1016/j.aej.2023.03.073

17. W. F. Alfwzan, M. H. DarAssi, F. M. Allehiany, M. A. Khan, M. Y. Alshahrani, E. M. Tag-eldin, A novel mathematical study to understand the lumpy skin disease (LSD) using modified parameterized approach, *Results Phys.*, **51** (2023), 106626. https://doi.org/10.1016/j.rinp.2023.106626

18. C. I. Siettos, L. Russo, Mathematical modeling of infectious disease dynamics, *Virulence*, **4** (2013), 295–306. https://doi.org/10.4161/viru.24041

19. M. Y. Li, *An introduction to mathematical modeling of infectious diseases*, Cham: Springer, 2018. https://doi.org/10.1007/978-3-319-72122-4

20. N. Mustafa, J. Ul Rahman, A. Omame, Modelling of Marburg virus transmission dynamics: a deep learning-driven approach with the effect of quarantine and health awareness interventions, *Model. Earth Syst. Environ.*, **10** (2024), 7337–7357. https://doi.org/10.1007/s40808-024-02169-y

21. F. Arif, Z. Majeed, J. Ul Rahman, N. Iqbal, J. Kafle, Mathematical modeling and numerical simulation for the outbreak of COVID-19 involving loss of immunity and quarantined class, *Comput. Math. Methods Med.*, **2022** (2022), 3816492. https://doi.org/10.1155/2022/3816492

22. D. Baleanu, M. Hasanabadi, A. M. Vaziri, A. Jajarmi, A new intervention strategy for an HIV/AIDS transmission by a general fractional modeling and an optimal control approach, *Chaos Solitons Fract.*, **167** (2023), 113078. https://doi.org/10.1016/j.chaos.2022.113078

23. F. B. Agusto, Optimal chemoprophylaxis and treatment control strategies of a tuberculosis transmission model, *World J. Model. Simul.*, **5** (2009), 163–173. Available from: `https://api.semanticscholar.org/CorpusID:716789`.

24. W. Ahmad, M. Abbas, Effect of quarantine on transmission dynamics of Ebola virus epidemic: a mathematical analysis, *Eur. Phys. J. Plus*, **136** (2021), 355. https://doi.org/10.1140/epjp/s13360-021-01360-9

25. A. Mannan, N. Shoket, J. Ul Rahman, R. Uwitije, Dynamic analysis of Ebola virus disease with non-linear incidence rate using morlet wavelet neural networks and hybrid optimization techniques, *Model. Earth Syst. Environ.*, **11** (2025), 79. https://doi.org/10.1007/s40808-024-02256-0

26. D. Baleanu, F. A. Ghassabzade, J. J. Nieto, A. Jajarmi, On a new and generalized fractional model for a real cholera outbreak, *Alex. Eng. J.*, **61** (2022), 9175–9186. https://doi.org/10.1016/j.aej.2022.02.054

27. A. I. K. Butt, M. Imran, S. Batool, M. A. Nuwairan, Theoretical analysis of a COVID-19 CF-fractional model to optimally control the spread of pandemic, *Symmetry*, **15** (2023), 380. https://doi.org/10.3390/sym15020380

28. N. Shoket, J. Ul Rahman, N. Zafar, Mathematical modeling and computational investigation of the COVID-19 epidemic using wavelet neural networks and coupled optimization, *Soft Comput.*, **29** (2025), 5859–5876. https://doi.org/10.1007/s00500-025-10916-1

29. Y. Li, M. Feng, L. J. Deng, M. Perc, J. Kurths, Digital epidemiology with awareness-based event-triggered migration in networked cyber-physical systems, *IEEE Trans. Netw.*, **34** (2026), 4885–4898. https://doi.org/10.1109/TON.2026.3688173

30. M. Feng, Y. Li, J. Kurths, Epidemic transmission modelling on the birth-death evolving network with indirect contacts, *Appl. Math. Model.*, **158** (2026), 116905. https://doi.org/10.1016/j.apm.2026.116905

31. S. Peng, M. Feng, L. J. Deng, M. Perc, J. Kurths, Information-epidemic dynamics in cyber-physical systems: a hypergraph framework with interpersonal relationships, *IEEE Internet Things J.*, **13** (2026), 39595–39609. https://doi.org/10.1109/JIOT.2026.3707111

32. O. D. Falowo, J. A. Owolabi, R. Akingbade, Mathematical modelling of lumpy skin disease in dairy cow, *IOP Conf. Ser. Earth Environ. Sci.*, **1219** (2023), 012007. https://doi.org/10.1088/1755-1315/1219/1/012007

33. R. Magori-Cohen, Y. Louzoun, Y. Herziger, E. Oron, A. Arazi, E. Tuppurainen, et al., Mathematical modelling and evaluation of the different routes of transmission of lumpy skin disease virus, *Vet. Res.*, **43** (2012), 1. https://doi.org/10.1186/1297-9716-43-1

34. B. Mat, M. S. Arikan, A. C. Akin, M. B. Çevrimli, H. Yonar, M. A. Tekindal, Determination of production losses related to lumpy skin disease among cattle in Turkey and analysis using SEIR epidemic model, *BMC Vet. Res.*, **17** (2021), 300. https://doi.org/10.1186/s12917-021-02983-x

35. N. H. Sweilam, W. A. Kareem, S. M. Al-Mekhlafi, M. M. A. Hasan, T. H. El-Ghareeb, T. M. Soliman, New crossover lumpy skin disease: numerical treatments, *Partial Differ. Equ. Appl. Math.*, **12** (2024), 100986. https://doi.org/10.1016/j.padiff.2024.100986

36. M. M. A. Hasan, A. M. Alghanmi, H. Al Ali, Z. Mukandavire, Improved numerical schemes to solve general fractional diabetes models, *Alex. Eng. J.*, **109** (2024), 29–40. https://doi.org/10.1016/j.aej.2024.08.095

37. M. M. A. Hasan, An efficient discretization scheme for a time-delay variable-order fractional diabetes model, *Math. Methods Appl. Sci.*, **49** (2026), 960–976. https://doi.org/10.1002/mma.70202

38. Y. LeCun, Y. Bengio, G. Hinton, Deep learning, *Nature,* **521** (2015), 436–444. https://doi.org/10.1038/nature14539

39. B. Yegnanarayana, *Artificial neural networks*, New Delhi: PHI Learning, 2009.

40. M. I. Jordan, T. M. Mitchell, Machine learning: trends, perspectives and prospects, *Science*, **349** (2015), 255–260. https://doi.org/10.1126/science.aaa8415

41. I. Goodfellow, Y. Bengio, A. Courville, *Deep learning*, Cambridge: MIT Press, 2016.

42. R. Szeliski, *Computer vision: algorithms and applications*, Cham: Springer, 2022. https://doi.org/10.1007/978-3-030-34372-9

43. O. I. Abiodun, A. Jantan, A. E. Omolara, K. V. Dada, N. A. Mohamed, H. Arshad, State-of-the-art in artificial neural network applications: a survey, *Heliyon*, **4** (2018), e00938. https://doi.org/10.1016/j.heliyon.2018.e00938

44. I. E. Lagaris, A. Likas, D. I. Fotiadis, Artificial neural networks for solving ordinary and partial differential equations, *IEEE Trans. Neural Netw.*, **9** (1998), 987–1000. https://doi.org/10.1109/72.712178

45. N. Yadav, A. Yadav, M. Kumar, *An introduction to neural network methods for differential equations*, Berlin: Springer, 2015. https://doi.org/10.1007/978-94-017-9816-7

46. D. R. Parisi, M. C. Mariani, M. A. Laborde, Solving differential equations with unsupervised neural networks, *Chem. Eng. Process.*, **42** (2003), 715–721. https://doi.org/10.1016/S0255-2701(02)00207-6

47. S. Mall, S. Chakraverty, Application of Legendre Neural Network for solving ordinary differential equations, *Appl. Soft Comput.*, **43** (2016), 347–356. https://doi.org/10.1016/j.asoc.2015.10.069

48. C. Michoski, M. Milosavljević, T. Oliver, D. R. Hatch, Solving differential equations using deep neural networks, *Neurocomputing*, **399** (2020), 193–212. https://doi.org/10.1016/j.neucom.2020.02.015

49. H. Kumar, N. Yadav, Deep learning algorithms for solving differential equations: a survey, *J. Exp. Theor. Artif. Intell.*, **37** (2023), 609–648. https://doi.org/10.1080/0952813X.2023.2242356

50. J. Wang, X. Peng, F. Yin, J. Yao, A deep neural network method for solving partial differential equations with complex boundary in groundwater seepage, *J. Pet. Sci. Eng.*, **209** (2022), 109880. https://doi.org/10.1016/j.petrol.2021.109880

51. J. Jin, J. Zhu, L. Zhou, C. Chen, L. Wu, M. Lu, A complex-valued variant-parameter robust zeroing neural network model and its applications, *IEEE Trans. Emerg. Top. Comput. Intell.*, **8** (2024), 1303–1321. https://doi.org/10.1109/TETCI.2024.3356163

52. J. Jin, W. Chen, A. Ouyang, F. Yu, H. Liu, A time-varying fuzzy parameter zeroing neural network for the synchronization of chaotic systems, *IEEE Trans. Emerg. Top. Comput. Intell.*, **8** (2024), 364–376. https://doi.org/10.1109/TETCI.2023.3301793

53. Y. Wu, Y. Yang, H. Nishiura, M. Saitoh, *Deep learning for epidemiological predictions*, New York: Association for Computing Machinery, 2018, 1085–1088. https://doi.org/10.1145/3209978.3210077

54. J. Ul Rahman, F. Makhdoom, U. Rashid, D. Lu, A. Akgul, M. K. Hassani, An oscillatory deep neural network for coupled electrical circuits, 2024. https://doi.org/10.21203/rs.3.rs-3936653/v1

55. J. Ul Rahman, S. Danish, D. Lu, Deep neural network-based simulation of Sel'kov model in glycolysis: a comprehensive analysis, *Mathematics*, **11** (2023), 3216. https://doi.org/10.3390/math11143216

56. M. Farhan, Waseem, A. Thaljaoui, M. U. Rahman, Data-driven investigation of an epidemic model under saturated incidence rate using deep neural networks, *J. Appl. Math. Comput.*, **11** (2025), 7983–8017. https://doi.org/10.1007/s12190-025-02639-1

57. M. Z. Meetei, R. Shafqat, A. H. Msmali, W. Hamali, Deep neural network applications in mathematical epidemiology: case of rabies virus, *AIMS Math.*, **10** (2025), 23261–23291. https://doi.org/10.3934/math.20251032

58. N. Mustafa, J. Ul Rahman, U. Ishtiaq, I. L. Popa, Artificial neural network-based approach for dynamic analysis and modeling of Marburg virus epidemics for health care, *Symmetry*, **17** (2025), 578. https://doi.org/10.3390/sym17040578

59. J. Ul Rahman, I. Noureen, A. Mannan, R. Uwitije, PhyFold: environment-aware physics-informed neural network for protein folding dynamics, 2025. https://doi.org/10.21203/rs.3.rs-8066072/v1

60. K. Janocha, W. M. Czarnecki, On loss functions for deep neural networks in classification, *Schedae Inform.*, **25** (2016), 49–59. https://doi.org/10.4467/20838476SI.16.004.6185

61. Q. Wang, Y. Ma, K. Zhao, Y. Tian, A comprehensive survey of loss functions in machine learning, *Ann. Data Sci.*, **9** (2022), 187–212. https://doi.org/10.1007/s40745-020-00253-5

62. J. Qi, J. Du, S. M. Siniscalchi, X. Ma, C. H. Lee, On mean absolute error for deep neural network-based vector-to-vector regression, *IEEE Signal Process. Lett.*, **27** (2020), 1485–1489. https://doi.org/10.1109/LSP.2020.3016837

63. L. Liu, P. Li, M. Chu, Z. Zhai, L2-loss nonparallel bounded support vector machine for robust classification and its DCD-type solver, *Appl. Soft Comput.*, **126** (2022), 109125. https://doi.org/10.1016/j.asoc.2022.109125

64. J. Ul Rahman, A. Ali, M. Ur Rehman, R. Kazmi, A unit softmax with Laplacian smoothing stochastic gradient descent for deep convolutional neural networks, In: I. S. Bajwa, T. Sibalija, D. N. A. Jawawi, *Intelligent technologies and applications*, Singapore: Springer, 2020, 162–174. https://doi.org/10.1007/978-981-15-5232-8_14

65. I. R. P. Selvam, S. C. Inunganbi, K. B. Anusha, G. Balakrishna, Mohebbanaaz, D. S. Rani, A deep learning framework for automated lumpy skin disease detection in cattle, *Adv. Anim. Vet. Sci.*, **14** (2026), 1231–1244. https://doi.org/10.17582/journal.aavs/2026/14.6.1231.1244

66. Z. Wang, Y. Li, X. Wang, W. Zhang, Y. Chen, X. Lu, et al., Precision strike strategy for liver diseases trilogy with Xiao-Chai-Hu decoction: a meta-analysis with machine learning, *Phytomedicine*, **142** (2025), 156796. https://doi.org/10.1016/j.phymed.2025.156796

67. H. Liu, P. Bing, M. Zhang, G. Tian, J. Ma, H. Li, et al., MNNMDA: predicting human microbe-disease association via a method to minimize matrix nuclear norm, *Comput. Struct. Biotechnol. J.*, **21** (2023), 1414–1423. https://doi.org/10.1016/j.csbj.2022.12.053

68. Z. Du, Y. Zeng, Z. Zhao, Y. Xu, M. Xu, M. Zhao, et al., Integrative approaches to uncover the therapeutic action of Huaiqihuang in myocarditis: network pharmacology, molecular docking, and molecular dynamics, *Curr. Pharm. Des.*, **32** (2026), 2932–2952. https://doi.org/10.2174/0113816128393399251021101651

69. W. Wang, Z. Liu, M. Li, J. Zheng, R. Zhang, K. Liu, et al., AIEgen-based proactive early warning system and precise treatment strategy for monkeypox prevention and control, *Adv. Sci.*, **13** (2026), e15865. https://doi.org/10.1002/advs.202515865

70. J. Qian, C. Wang, H. Wu, Q. Chen, C. Zuo, Ensemble deep learning-enabled single-shot composite structured illumination microscopy (eDL-cSIM), *PhotoniX*, **6** (2025), 13. https://doi.org/10.1186/s43074-025-00171-w

71. J. Pan, Z. Liu, X. Li, X. Luo, F. Huang, M. He, et al., An end-to-end dual backbone framework for UAV fish disease detection using optimized GateHCO feature fusion mechanism, *Neural Netw.*, **203** (2026), 109140. https://doi.org/10.1016/j.neunet.2026.109140

72. Y. Chi, H. Xiao, S. Wei, Y. Wang, Z. Zhang, M. M. Nadakatti, MAGSE-ResNet50: a deep learning approach for railway sandy ballast fouling detection, *Measurement*, **282** (2026), 122023. https://doi.org/10.1016/j.measurement.2026.122023

73. *Food and Agriculture Organization of the United Nations, Appendix 18. Smallholder dairy production parameters, as used in LDPS2 modelling*, FAO, Available from: https://www.fao.org/4/y4176e/y4176e0u.htm.

74. G. Mani, A. J. Gnanaprakasam, S. Ramalingam, A. S. A. Omer, I. Khan, Mathematical model of the lumpy skin disease using Caputo fractional-order derivative via invariant point technique, *Sci. Rep.*, **15** (2025), 9112. https://doi.org/10.1038/s41598-025-92884-y

75. A. I. K. Butt, H. Aftab, M. Imran, T. Ismaeel, M. Arab, M. Gohar, et al., Dynamical study of lumpy skin disease model with optimal control analysis through pharmaceutical and non-pharmaceutical controls, *Eur. Phys. J. Plus*, **138** (2023), 1048. https://doi.org/10.1140/epjp/s13360-023-04690-y

76. P. van den Driessche, Reproduction numbers of infectious disease models, *Infect. Dis. Model.*, **2** (2017), 288–303. https://doi.org/10.1016/j.idm.2017.06.002

77. W. Liu, X. Chen, D. Miao, H. Zhang, X. Qin, S. Du, et al., SEAD-MGFE-Net: Schrödinger equation-based adaptive dropout multi-granular feature enhancement network for conversational aspect-based sentiment quadruple analysis, *Inf. Sci.*, **723** (2026), 122684. https://doi.org/10.1016/j.ins.2025.122684



AIMS Press

© 2026 the Author(s), licensee AIMS Press. This is an open access article distributed under the terms of the Creative Commons Attribution License (https://creativecommons.org/licenses/by/4.0)